

Studiengang

**Applied Life Sciences**

PO Version 2016

**Bachelorarbeit**

**Characterization of the Current-Driven Organic Electrochemical Transistor with an integrated Barrier Tissue and its Application in sensing reversible Tight Junction Modulation**

Charakterisierung des Current-Driven Organischen Elektrochemischen Transistors mit integriertem Epithelgewebe und seine Anwendung zur Erfassung einer reversible Tight Junction Modulation

vorgelegt von

**Daria Harig**

Am 16. März 2021

Betreuung: Prof. Dr. Hildegard Möbius

Zweitkorrektur: Prof. Dr. Marko Baller



---

## Abstract

The passage of nutrients into the blood circulation or locally to target organs is regulated by the barrier functionality of epithelial barrier tissues. Particularly, tight junctions seal the paracellular transport across these barriers, impeding the passage of, e.g. hydrophilic drugs.

The increasing development of novel chemicals and drugs enhances the need of replacing the animal model by well-established sensing technology utilizing *in vitro* human tissue. The ability of barrier tissue to impede the passage of ions or drugs through it, is described as its barrier function. For drug targeting, external chemical agents regulate the barrier function of tissues by reversibly opening tight junctions. The barrier function can be electrically assessed by measuring the resistance across the cell layer. Here, the transient behavior of the OECT with integrate barrier tissue, comparing the OECT in the standard and current-driven configuration, is investigated. Further, the OECT is used in the current-driven configuration to investigate reversible modulation of tight junctions in CaCo-2 and MDCKII barrier tissues over time. The tight junction modulation is induced in a concentration-dependent matter, by exposure to a low and high concentration of ethylenediaminetetraacetic acid (EDTA). The results demonstrate the suitability of OECTs with integrated barrier tissue to *in situ* monitor temporal barrier modulation and recovery, which can offer valuable information for drug delivery applications.



---

## Kurzfassung

Der Transport von Nährstoffen in den Blutkreislauf oder lokal zu Zielorgan wird durch die Barrierefunktion von epithelialen Barrieregeweben reguliert. Insbesondere so genannte Tight Junctions dichten den parazellulären Transport durch diese Barriere ab und erschweren somit die Passage von, zum Beispiel, hydrophilen Wirkstoffen.

Die zunehmende Entwicklung neuartiger Chemikalien und Medikamenten verstärkt die Notwendigkeit Tiermodelle durch eine etablierte Sensortechnologie, unter Verwendung von menschlichem *in vitro* Gewebe, zu ersetzen. Die Fähigkeit von Barrieregewebe, den durchtritt von Ionen oder Medikamente zu verhindern, wird als Barrierefunktion bezeichnet. Bei gezielter Medikamentenabgabe regulieren externe chemische Wirkstoffe die Barrierefunktion von Geweben, indem sie die Tight Junctions reversibel öffnen. Die Barrierefunktion kann durch Messung des Widerstands über die Zellschicht elektrisch bewertet werden. Hier wird das transiente Verhalten des OECT mit integriertem Barrieregewebe untersucht, wobei der OECT in der Standard- und *Current-Driven* Konfiguration verglichen wird. Weiterhin wird der OECT in der Current-Driven Konfiguration verwendet, um die reversible Modulation der Tight Junctions in CaCo-2 und MDCKII Barrieregeweben über die Zeit zu untersuchen. Die Modulation der Tight Junctions wird konzentrationsabhängig durch die Exposition mit einer niedrigen und einer hohen Konzentration von Ethylendiamintetraessigsäure (EDTA) induziert. Die Ergebnisse zeigen die Eignung von OECTs mit integriertem Barrieregewebe zur in situ Überwachung der zeitlichen Barriere Modulation und -Regeneration, was wertvolle Informationen für Anwendungen zur Medikamentenabgabe liefern kann.



---

## Declaration of Authorship

I, **Daria Harig**, born on the **1<sup>st</sup> of February 1999 in Neunkirchen-Saar**, hereby declare on my word of honor that I have completed my bachelor thesis with the title:

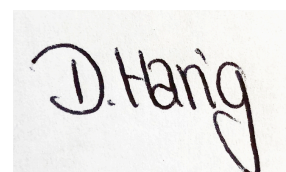
**Characterization of the Current-Driven Organic Electrochemical Transistor with an integrated Barrier Tissue and its Application in sensing reversible Tight Junction Modulation**

Independently and without external help and have not used any other means of assistance other than those specified in the thesis.

I have marked the adoption of literal quotations from literature as well as the use of other authors thoughts at the appropriate places within the thesis. I am aware that an incorrect statement can have legal consequences

Mainz, 16.03.2021

Daria Harig

A photograph of a handwritten signature in black ink on a light-colored surface. The signature reads "D. Harig" in a cursive, slightly slanted script. The "D" is a simple circle with a vertical line, and the "Harig" is written in a fluid, connected hand.





---

## Acknowledgements

I thank Prof. Paul Blom and Dr. Paschalis Gkoupidenis, for giving me the opportunity to work in an inspiring working group and impressive environment as the Max-Planck Institute in Mainz. Further, I want to give my regards to Dr. Paschalis Gkoupidenis for giving me such an interesting and challenging project to work on and for the time you always found for discussions and assistance.

I would like to thank Prof. Dr. Möbius and Dr. Jasper Michels for introducing me to the Max-Planck Institute. Particularly, I would also like to thank Prof. Dr. Möbius for supervising my thesis as the first reviewer and Dr. Jasper Michels for challenging my mathematical skills and guiding me through the new territory of modelling.

Further, I want to express by sincere thanks to Maximilian Brückner for introducing me to cell culturing and to the cLSM! Thank you for patiently teaching me all the biology-related lab work!

Very special gratitude goes to my supervisor Katharina Lieberth, who met me on equal footing and provided me with the necessary skills, I was able to build on. You gave me respect and trust to work independently but also guidance, anytime I needed it. Also thank you for answering my endless questions and bringing structure to my thoughts, any time of the day! I will definitely miss our lab conversations, which occasionally went beyond scientific discussions.

In addition, I want to thank the rest of AK Blom, it was a pleasure to work in such a supportive and warm atmosphere.

Thank you!



---

# Table of contents

Abstract .....	iii
Kurzfassung.....	v
Declaration of Authorship .....	vii
Acknowledgements .....	ix
List of Figures .....	xiii
List of Tables .....	xiii
Glossary .....	xv
Abbreviations.....	xvii
<b>1. Introduction .....</b>	<b>1</b>
<b>1.1 Conductive Polymer based Bioelectronics .....</b>	<b>1</b>
<b>1.2 The Highly Conductive Polymer Poly(3,4-ethylenedioxythiophene) and its Dopant Poly(styrene sulfonic acid) .....</b>	<b>3</b>
<b>1.3 Organic Electrochemical Transistors .....</b>	<b>5</b>
<b>1.3.1 The Organic Electrochemical Transistor in the Current-Driven Configuration .....</b>	<b>7</b>
<b>1.4 Epithelial Cells and Cell Junctions.....</b>	<b>9</b>
<b>2. Motivation and Outline .....</b>	<b>15</b>
<b>3. Experimental .....</b>	<b>17</b>
<b>3.1 Material .....</b>	<b>17</b>
Chemicals .....	17
Consumables .....	18
<b>3.2 Methods.....</b>	<b>19</b>
<b>3.2.1 Device Fabrication of Organic Electrochemical Transistors.....</b>	<b>19</b>
<b>3.2.2 Cell Preparation .....</b>	<b>20</b>
<b>3.2.2.1 Cell Culturing of CaCo2 and MDCK II Cells.....</b>	<b>20</b>
<b>3.2.2.2 Filter Preparation .....</b>	<b>21</b>
<b>3.2.3 Impedance Spectroscopy for Cell Layer Characterization .....</b>	<b>22</b>
<b>3.2.4 OECT Operation .....</b>	<b>22</b>

---

3.2.4.1 Transfer Characteristics .....	23
3.2.4.2 Transient Response measurement in standard OECT configuration.....	23
3.2.4.3 Transient Response Measurement with the OECT in Current-Driven configuration.....	23
3.2.5 Trans Epithelial Electrical Resistance Measurement of CaCo2 and MDCK II Cells .....	23
3.2.6 Immunofluorescence Staining to Visualize Tight Junctional Proteins.....	23
3.2.7 Detecting Tight Junction Modulation with the OECT in the Current-Driven configuration .....	24
<b>4. Results and Discussion.....</b>	<b>25</b>
4.1 Characterization of Barrier Tissue with Electrochemical Impedance Spectroscopy of the Organic Electrochemical Transistor .....	25
4.2 <i>Investigating the Transient Characteristics of an Organic Electrochemical Transistor with an integrated Barrier Tissue</i> .....	28
4.2.1 Probing Transient Response Measurements in Standard Organic Electrochemical Transistor Configuration with a specific scan rate .....	28
4.2.2 Examine Transient Response Measurements in Current-Driven Organic Electrochemical Transistor Configuration with a changing scan rate.....	31
4.1 <i>Biological Application of the OECT in the Current-Driven Configuration</i> .....	34
4.1.1 Immunofluorescence Staining of Tight Junctional Proteins .....	34
4.1.2 Detecting Tight Junction Modulation of CaCo2 and MDCK II with the OECT.....	36
<b>5. Summary and Outlook.....</b>	<b>41</b>
<b>6. Appendix.....</b>	<b>43</b>
<b>7. References.....</b>	<b>49</b>

---

## List of Figures

Figure 1: Chemical structure of PEDOT:PSS.....	3
Figure 2: Comparison of different transistor technologies.....	5
Figure 3: Device structure of a PEDOT:PSS based OECT.....	6
Figure 4: Device architecture in the current-driven configuration and corresponding electrical characteristics.....	8
Figure 5: Schematic illustration of epithelial tissue anchored to the extracellular matrix..	10
Figure 6: Schematic illustration of tight junction proteins .....	11
Figure 7: Schematic illustration of the fabricated device sample.....	19
Figure 8: Filter preparation .....	21
Figure 9: device architecture of an organic electrochemical transistor with integrated filter. ....	22
Figure 10: Electrochemical Impedance Spectra of barriers of varying impedance .....	25
Figure 11: Overview of capacitance and resistance values contributing to the total impedance and equivalent circuit. ....	26
Figure 12: Transient response of the electronic current with the OECT in the standard configuration. ....	28
Figure 13: Transient response of the ionic current with the OECT in the standard configuration .....	29
Figure 14: Comparison of transient electronic current $I_D$ and ionic charge density $Q$ over time. ....	30
Figure 15: Transient Response of the OECT in the Current-Driven Configuration with different integrated barriers.....	32
Figure 16: CLSM images of CaCo-2 barrier tissue.....	34
Figure 17: CLSM Images of MDCKII barrier tissue .....	35
Figure 18: Concentration effect of TJ modulator to MDCKII cells, measured with the current-driven OECT.....	36
Figure 19: Concentration effect of TJ modulator EDTA to CaCo-2 cells, measured with the current-driven OECT.....	37

## List of Tables

Table 1: List of Antibodies .....	18
Table 2: List of Cell lines .....	18



---

## Glossary

<b>OECT</b>	Organic Electrochemical Transistor
<b>OFET</b>	Organic Field-Effect Transistor
<b>EGOFET</b>	Electrolyte-Gated Field-Effect-Transistor
<b>PEDOT</b>	Poly(3,4-ethylenedioxythiophene)
<b>PSS</b>	Poly(styrene sulfonic acid)
<b>DMSO</b>	Dimethyl Sulfoxide
<b>DBSA</b>	4-Dodecylbenzenesulfonic acid
<b>GOPS</b>	(3-glycidyloxypropyl)-trimethoxy silane
<b>EMEM</b>	Eagle's Minimum Essential Medium
<b>FBS</b>	Fetal Bovine Serum
<b>PBS</b>	Phosphate buffered salt solution
<b>PFA</b>	Paraformaldehyde
<b>PDMS</b>	Polydimethylsiloxane
<b>TEER</b>	Transepithelial Electrical Resistance
<b>PMMA</b>	Poly(methyl methacrylate)
<b>EDTA</b>	Ethylenediaminetetraacetic acid
<b>UV</b>	Ultraviolet
<b>EIS</b>	Electrochemical Impedance Spectroscopy
<b>TJ</b>	Tight Junction
<b>cLSM</b>	Confocal laser scanning microscopy





---

## Abbreviations

$V_G$	Gate voltage
$V_D$	Drain voltage
$V_S$	Source voltage
$I_D$	Drain current
$V_{in}$	Input voltage
$V_{out}$	Output voltage
$I_B$	Current bias
$V_{DD}$	Voltage compliance
$r_o$	Output resistance
$V_{SW}$	Switching voltage
$g_m$	Transconductance
$W$	Width
$L$	Length
$D$	Thickness
$C_V$	Volumetric capacitance
$q$	Elementary charge
$P_0$	Density
$\mu$	Charge carrier mobility
$\beta$	Current prefactor
$R_{EL}$	Resistance of the electrolyte
$R_{MEM}$	Resistance of the cell membrane
$C_{MEM}$	Capacitance of the cell membrane
$C_{CH}$	Capacitance of the channel



# 1. Introduction

This chapter introduces bioelectronics, its general concept and achievements since the discovery and establishment of this field in the 18<sup>th</sup> century. The most important devices and materials, shaped on this trail, are examined in more detail, which particularly includes the conductive polymer Poly(3,4-ethylenedioxythiophene) (PEDOT) and the organic electrochemical transistor (OECT). The chapter concludes with an excursion into biology, as epithelial tissues and tight junctions become essential in this work.

## 1.1 Conductive Polymer based Bioelectronics

The realm of bioelectronics is a strong emerging field that dates back to the 18th century. At the University of Bologna, Luigi Galvani set the trail for bioelectronics with his work.<sup>[1,2]</sup> Galvani used bioelectronic forces to study living organisms. In his now famous experiment, he made a detached leg of a frog twitch by applying voltage.<sup>[2]</sup> An age of enlightenment, introduced by Galvani's work, brought a better understanding of communication between electronics and the world of biology.<sup>[3]</sup> Ever since, the field of bioelectronics experienced a tremendous growth. Today, there are a variety of bioelectronic devices that are used for medical diagnostics and therapy. Examples are glucose sensors for diabetes, cochlear implants or defibrillators, just to name a few of the most prominent devices emerged from these studies.<sup>[1,2,3,4]</sup> Other bioelectronic devices are utilized in research, to e.g. capture simulations and models about the human brain<sup>[5]</sup> or to get a better understanding of how cells communicate with their environment.<sup>[2]</sup>

Bioelectronics represent the branch of science concerned with the development of translatable systems to selectively monitor biological signals or phenomena and convert them into a corresponding readout for electronic processing devices.<sup>[4]</sup> These devices are able to operate in dual direction. On one hand, the device is able to sense biological signals and transduce it to an electrical parameter such as impedance, potential, or electronic current. On the other hand, the electronic system itself controls biological microsystems, such as biomolecular processes and cells as well as macrosystems, such as tissues and organs.<sup>[6]</sup>

The development of bioelectronic devices in the last decade has offered a variety of utilized materials, especially metal based devices were state of the art for a few years. As a result, numerous metal electrode based wearable and implantable devices, such as frequency stimulating biosensors for Deep Brain Stimulation have been developed.<sup>[3,7]</sup> Even though well established biosensors emerged from these studies, metals suffer from biological incompatibility and inefficient transduction of biological to electrical signals.<sup>[2]</sup> Since mother nature has processed the most effective catalysts (enzymes), biomolecules with highly specific binding capabilities (antibodies) and the fastest computing system

(nerves), it is up to humankind and technical development to discover novel materials having equivalent properties.<sup>[6]</sup> One material emerging from these studies are hydrogels, crosslinked polymer networks permeated with water. The similarity of hydrogels to biological systems has attracted attention in bioelectronics. Especially the field of epidermal bioelectronics benefits from hydrogels, e.g. long-term conformal electromyography (EMG)<sup>[3]</sup> and electronic skin to mimic native tissue.<sup>[8]</sup>

The flexible and soft nature of hydrogels as well as their ion-rich physiological environment offers an ideal biocompatibility and minimizes mechanical mismatch. Hydrogels are considered as the communication bridge between biology and electronics, since biological events take place in aqueous environment with ions as charge carriers, whereas electronics are dry and rely on electrons as charge carriers. Especially the oxide-free interface of hydrogels with aqueous electrolyte and the signal transmission through the whole volume of the hydrogel film, not just on the surface, has proved to be the key advantage of hydrogels. While the amount of new hydrogel based applications grew, a disadvantage arose during these studies. Hydrogels lack electronic conductivity and their ionic conductivity is up to nine magnitudes lower than the conductivity of metals.<sup>[3,9]</sup> However, hydrogels based on conductive polymer networks, such as Poly(3,4-ethylenedioxythiophene):Poly(styrene sulfonic acid) (PEDOT:PSS), offer high electronic and ionic conductivity and therefore not only bridge the gap between ionic signal transmission in biological systems and electronic signal transmission in electronic systems, but also offer efficient signal transmission and high conductivity.<sup>[3,10,11]</sup> Finally, this material stands out truly as unique due to ease in tuning properties, low-cost fabrication as well as aqueous-based green synthesis, flexibility and transparency.<sup>[10,12,13]</sup> Conductive polymers, infiltrated with water have endowed the field of bioelectronics with a variety of new applications, ranging from devices to record electrical activity of neurons to biomedical instruments.<sup>[2,14]</sup> In any case, one can say that with conductive polymer networks, a next generation of bioelectronics is developing.<sup>[3]</sup>

Throughout the years, numerous bioelectronic devices have been developed with applications such as stimulating and sensing of living organisms, or drug delivery systems established for medical diagnostics, therapy or living science. Just to name a few of these excellent tools: micro electrode arrays, organic field-effect transistors (OEFT's), and electrochemical devices, such as electrolyte-gated field-effect transistors (EGOFET'S), and ionic diodes.<sup>[2,4,15]</sup>

One of the most promising devices is the organic electrochemical transistor (OECT), based on the conductive polymer PEDOT:PSS. The OECT and its application in biology will be outlined in detail in the next sections.

## 1.2 The Highly Conductive Polymer Poly(3,4-ethylenedioxythiophene) and its Dopant Poly(styrene sulfonic acid)

Hydrogels of conductive polymer have been regarded as the most prominent device platforms for bioelectronics, since their great chemical versatility allows modification of their electrical, mechanical and optical properties.<sup>[16]</sup> The most frequently used polymer is Poly(3,4-ethylenedioxythiophene) (PEDOT).<sup>[17]</sup> Besides its insolubility, the electroactive PEDOT offers highly desirable properties such as mixed ionic and electronic conductivity, transparency, electrochemical stability in aqueous solution, and retaining its activity in a wide pH range.<sup>[17,18,19]</sup> PEDOT provides high hole conductivity, depending on the morphology, its dopant, and additives. The highest conductivity reported for PEDOT formulations is  $900 \text{ Scm}^{-1}$ .<sup>[18]</sup>

Due to PEDOT's insolubility, a stable water dispersion is generally created by introducing PEDOT to an anionic polymer. The most common form of PEDOT is a formulation doped with the water-dispersible polyelectrolyte poly(styrene sulfonic acid) (PSS). The negatively charged PSS not only enhances PEDOT'S conductivity, by allowing water uptake and swelling in water, it also allows a better processability.<sup>[10]</sup> The chemical structure of PEDOT:PSS is shown in **Fig.1**. PEDOT consists of a thiophene backbone and  $\pi$ -conjugated chains. PSS serves as the counterion to balance the oxidatively positive (p-type) doped PEDOT.

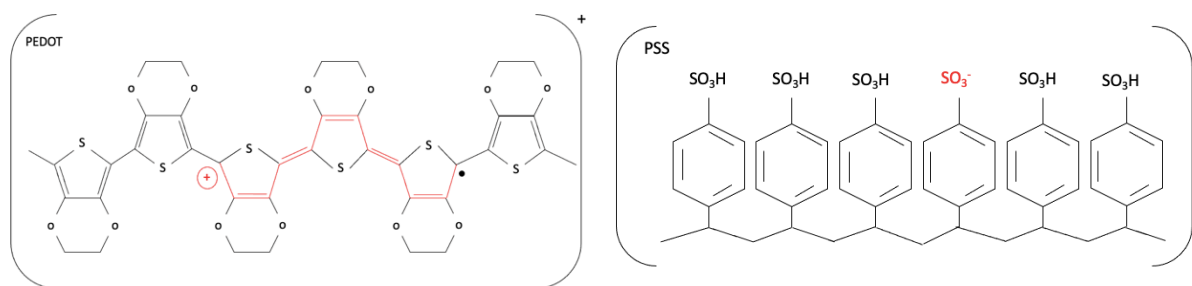


**Figure 1: Chemical structure of PEDOT:PSS.**

The illustration shows the molecular structure of positively doped [PEDOT]<sup>+</sup> and its dopant [PSS].

The PEDOT to PSS ratio determines morphology and conductivity, due to insulating properties of PSS and PEDOT's charge density. Dispersion properties are further regulated by water content and the particle size of PEDOT:PSS dispersions in water.<sup>[18]</sup> Typically, 1-5 % of PEDOT:PSS is in an aqueous colloidal dispersion with water, which allows film fabrication with common methods, such as spin-coating.<sup>[18]</sup> In dispersion, PEDOT:PSS tends to form micellar grains with a PEDOT core, embedded in a hydrophilic PSS body.<sup>[9]</sup> However, in PEDOT:PSS films, PSS forms an amorphous, hydrophilic matrix throughout the whole volume of the film. Gel-like, entangled PEDOT grains are embedded in this matrix, whereby the mobile holes in PEDOT are compensated by the negatively charged sulfonate

groups in PSS.<sup>[10,17]</sup> The amorphous property of PEDOT:PSS films allows ions from an electrolyte to penetrate the film, which is a process a variety of devices rely on.<sup>[11]</sup> Due to ion uptake and their uniform distribution throughout the whole volume of the film, the PEDOT:PSS capacitance is considered volumetric, implementing the linear relationship between capacitance and volume.<sup>[9,11,20]</sup>

Within PEDOT:PSS films, there are various molecular interactions, which cause the sidechains of the polymer blend to entangle. In between the p-type doped PEDOT and the negatively charged PSS chains, there are electrostatic forces, as well as  $\pi$ - $\pi$ -stacking of the PEDOT chains and entanglement within the PSS chains.<sup>[9]</sup> Since these interactions lead to decreased conductivity within the volume of the film, organic solvents, such as dimethyl sulfoxide (DMSO) or ethylene glycol, are added to increase conductivity by two to three orders of magnitude.<sup>[10,18,17,19]</sup> The addition of additives, such as organic solvents is termed as secondary doping.<sup>[19]</sup> Organic solvents change the conformation of PEDOT chains, due to interactions between the solvent's dipoles and the p-type doped PEDOT chains.<sup>[10]</sup> This conformational change generates linear PEDOT chains and modest separation between the highly conductive PEDOT and insulating PSS matrix. With this change in film morphology, a better transport of mobile charge carriers and, thus, a higher conductivity of the PEDOT:PSS film is achieved. A similar process occurs during PEDOT:PSS swelling in water, leading to an increase in conductivity.<sup>[9,17]</sup>

For better processability whilst spin-coating, surfactants, e.g. 4-Dodecylbenzenesulfonic acid (DBSA), are commonly used as secondary dopant, to increase its wetting behavior of PEDOT:PSS films on hydrophobic surfaces.<sup>[19,21,22]</sup> Furthermore, PEDOT:PSS dispersions can be treated with crosslinkers, such as (3-glycidyloxypropyl)-trimethoxy silane (GOPS). The crosslinker reacts with the sulfonic acid group of PSS and leads to enhanced matrix stability, which is preferred when operating over long-time with aqueous electrolyte. As a trade-off, crosslinker reduce ion mobility, conductivity and ability to swell in water. However, the decrease in conductivity can be compensated with optimized film geometry parameters.<sup>[16]</sup>

To sum up, the popularity of PEDOT:PSS arises from many advantageous properties, such as high conductivity, transparency, ability to swell in water, biocompatibility, tunability, processability, and being a mixed ionic-electronic conductor. Furthermore, the polymer blend has similar softness as tissue, offering a broad range of applications in epidermal bioelectronics. PEDOT:PSS has taken a remarkable place in the field of bioelectronics and has been used for versatile biomedical applications, such as implantable devices for electrophysiological recordings and glucose sensors.<sup>[1,10,23]</sup> PEDOT:PSS is with more than 15000 publications per year, one of the most studied materials on earth.<sup>[24]</sup> It got incredible attendance with the rise of bioelectronics and the introduction of the organic electrochemical transistors (OECT).<sup>[1,10,25]</sup>

### 1.3 Organic Electrochemical Transistors

Organic Bioelectronics, based on conductive polymers, provide a unique platform for coupling electronics and biological systems. A novel technology, leveraging the property of mixed electronic and ionic transport, is the PEDOT:PSS based organic electrochemical transistor (OECT).<sup>[25,26]</sup> Since it has been introduced first in 1984, the OECT has attracted considerable interest, especially in the field of bioelectronics.<sup>[27,28]</sup> The operation of OECT's relies on ion uptake into the conductive PEDOT:PSS channel, resulting in a high transconductance  $g_m$ , compared to other transistor technologies such as OFETs or EGOFETs (**Fig.2**).

The OFET is assembled by two electrodes, connected via an electronic conducting channel, which is in direct contact with a dielectric and a metal electrode on top, serving as the gate. In this system, the capacitance is determined by the thickness of the dielectric layer, which is different from the other field-effect transistor (FET) technologies. Upon an applied gate voltage, either electrons, in case of an n-type conducting channel, or holes, in case of a p-type conducting channel, accumulate at the channel-dielectric interface. The accumulation of mobile charge carriers at the interface is also referred to as field-effect and represents the basic working principle of FET technologies. The EGOFET is based on the same stacked structure, but here an electrolyte is an essential component of the system.<sup>[26]</sup> Upon an applied gate voltage hydrated ions from the electrolyte migrate to the electrolyte-channel interface to compensate the accumulated charge carriers at the channel interface. An electrical double layer is formed (**Fig.2**).<sup>[29,12]</sup>

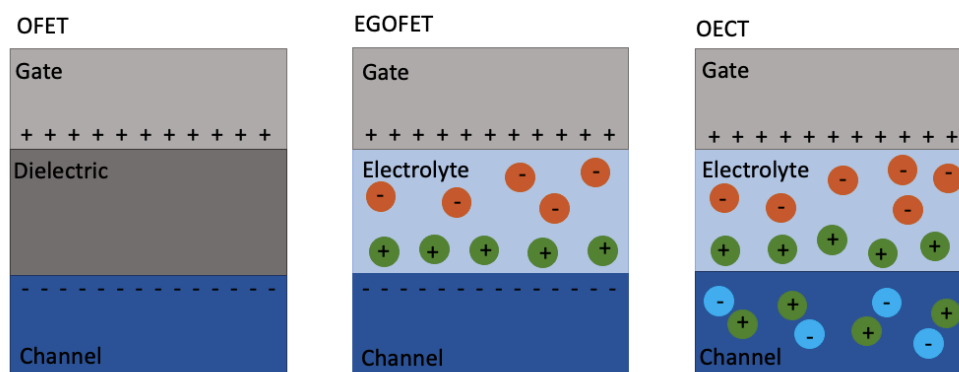


**Figure 2: Comparison of different transistor technologies.**

Device structure and charge carrier accumulation in different transistor technologies. In OFETs, mobile charge carriers of the channel accumulate at the dielectric interface, whereas mobile charge carriers in EGOFETs build an electrical double layer. In comparison, the current modulation in the OECT's channel is induced by an electrochemical reaction.

The OECT consists of a similar device structure, yet has one key difference. Since the OECT is based on PEDOT:PSS as conductive channel, the capacitance of the device is volumetric, whereas in EGOFET's, the area of the electrical double layer defines the capacitance. The operating principle of the OECT in

the standard configuration relies on generating a drain current  $I_D$  in the channel, as response to a potential difference  $V_{DS}$ . The quantity of mobile holes in the channel is proportional to  $V_{DS}$ , which is probing the channels doping state.<sup>[23]</sup> The gate electrode is crucial, as it drives the ions and modulates the magnitude of  $I_D$ , by doping and dedoping the PEDOT:PSS.<sup>[2,26]</sup>

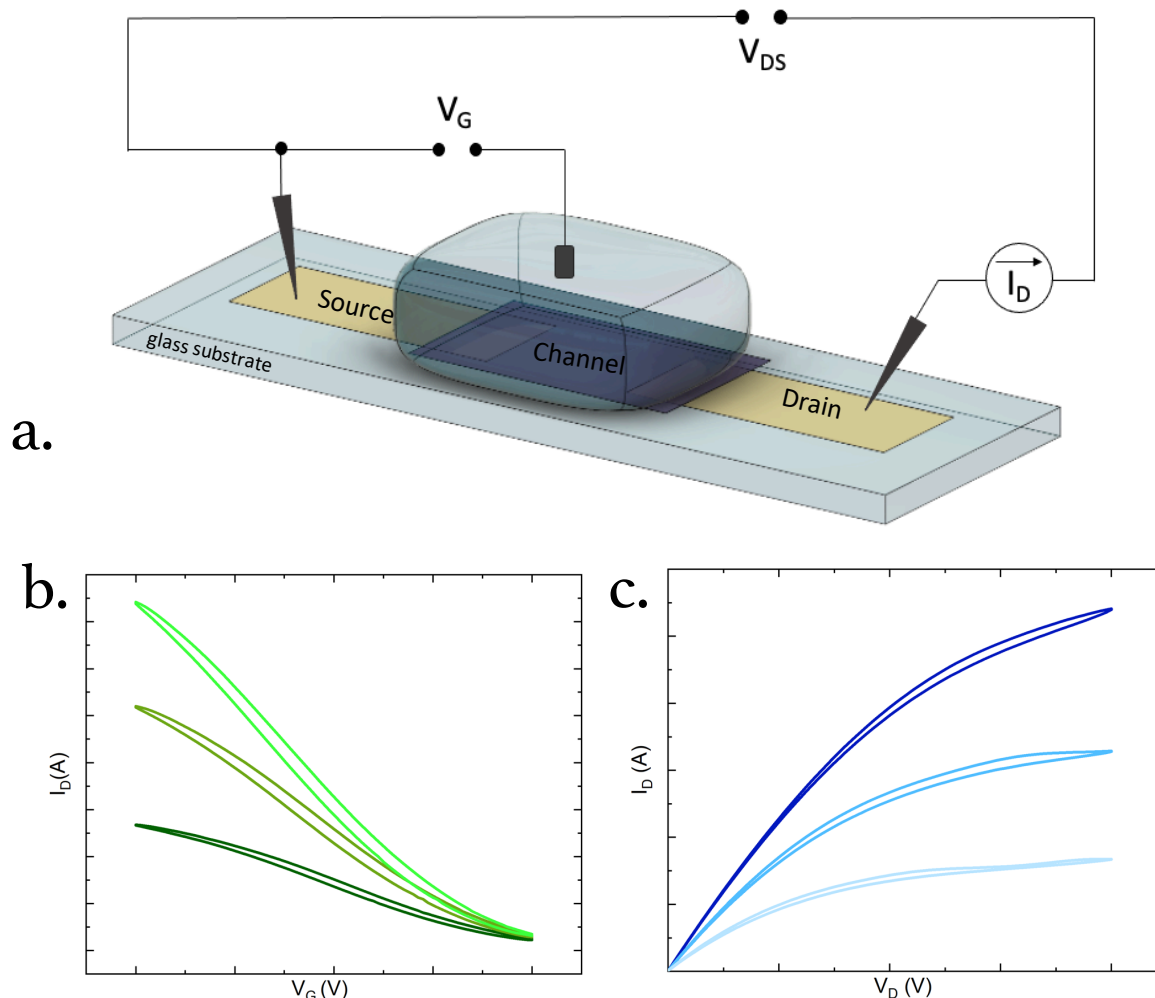


**Figure 3: Device structure of a PEDOT:PSS based OECT and electrical characteristics.**

a) Source and drain electrodes are connected via the conductive channel, PEDOT:PSS. Channel, as well as the source and drain are located on a glass substrate. The gate electrode is immersed into an electrolyte. Source and drain are connected to a Semiconductor Characterization system via pins. Source is grounded and a drain voltage  $V_{DS}$  is applied in respect to the source. b) The transfer characteristics show the forward and backward sweep of  $I_D$  at a specific for a series of  $V_D$ . c) Output characteristics show the forward and backward sweep of  $I_D$  for a series of  $V_G$ .

By applying a positive gate voltage  $V_G$ , anions of the electrolyte accumulate at the gate and cations migrate homogeneously over the whole channel volume. The negatively charged PSS-anions get compensated by the cations from the electrolyte, replacing PEDOT-holes. As PEDOT:PSS gets dedoped,  $I_D$  decreases. Once most PSS-anions are compensated with cations, the transistor reaches saturation in the OFF-state.<sup>[12,30,31]</sup> This process is reversible and can recover by ions drifting out of the



channel. By applying a negative  $V_G$ , cations are progressively extracted from the PEDOT:PSS and anions penetrate the channel, thus,  $I_D$  increases. In this way, the OECT transduces ionic signals to electronic current, labeled as ion-to-electron converting. The OECT can also be viewed as an amplifier, in which a low  $V_G$  is amplified on the way to the output, resulting in large modulation of  $I_D$ . OECTs identifying characteristics, that doping changes process over the whole bulk of channel, is a major advantage over EGFETs, where doping occurs along a thin interfacial region. [2,17]

The mechanism of amplification can be displayed in output ( $I_D - V_{DS}$ ) and transfer characteristics ( $I_D - V_G$ ) of the device. The efficiency of the process is described as the transconductance  $g_m$ , which is defined as the derivation of the transfer curve and calculated as:  $g_m = \Delta I_D / \Delta V_G$ . Typical transconductance values for OECTs reach a value of three order higher than other transistor technologies.[31]

The many advantages of the OECT have created a promising candidate for bioelectronics. Especially the low voltage operation, biocompatibility, and simple device architecture, allowing for ease in fabrication and miniaturizations offer a broad range of applications in the field of neural activity sensing, analyte detection, and impedance sensing.[31] Regarding the latter, irreversible disruption with e.g. hydrogen peroxide[32] or EGTA[15] have already been successfully monitored. More recently, the sensitivity of OECTs have been even enhanced at low voltages, using it in a current-driven, inverter-like configuration (1.3.1), offering advantageous properties in regard to biological applications.[33]

### 1.3.1 The Organic Electrochemical Transistor in the Current-Driven Configuration

The ion density in aqueous electrolyte plays a crucial role in terms of electrical charge, osmolarity and ion permeability, para or transcellular, across cell membranes and layers.[34] Therefore, *in vitro* quantification of ion concentration in electrolyte solutions is of great importance for biomedical applications.[33] The above described OECT standard configuration suffers from an intrinsic trade-off between sensitivity and operating voltage, but if used in the current-driven configuration (**Fig.8a**), the device overcomes these boundaries.[27,33]

For the OECT in the current-driven configuration an inverter topology is used:  $V_G$  refers to  $V_{in}$ ,  $V_{DS}$  refers to  $V_{out}$ . PEDOT:PSS doping state is modulated by an input voltage  $V_{in}$ , applied at the gate. The output voltage  $V_{out}$  is measured at the drain. (**Fig.8b**). An external current generator is connected to the drain, that forces a current bias  $I_B$ . The current generator incorporates a voltage  $V_{DD}$  with a specific compliance, which sets the measurable  $V_{out}$  range, given by equation (1).[27,33]

$$V_{out} = V_{DD} - I_B * r_o \quad (1)$$

Once a negative  $V_{in}$  is applied, anions are injected into the PEDOT:PSS, the polymer is doped and the channels output resistance  $r_o$  is small. The OECT operates in linear regime. With an increase of  $V_{in}$ , anions are progressively extracted from the PEDOT:PSS and cations migrate into the polymer,

dedoping PEDOT. With the decrease in conductivity,  $r_o$  increases and  $V_{out}$  decreases, until saturation is reached. Taking equation (1) into account, knowing that negative biased  $V_{in}$  results in low  $r_o$  and positive  $V_{in}$  in high  $r_o$ , one can say that  $V_{out}$  gets pushed towards  $+V_{DD}$  with negative  $V_{in}$  and small  $I_B$  and vice versa towards  $-V_{DD}$  for positive  $V_{in}$  (**Fig.8c**).<sup>[33]</sup> Simplified, it can be said that applying higher  $V_{in}$  ranges can be counteracted with a higher  $I_B$ , overcoming the limitation of the system by the supply voltage. Thus the OECT in the current-driven configuration not only allows low-voltage operation but also offers high ion sensitivity.<sup>[27,35]</sup> In this way dynamical processes of ion concentration in the electrolyte can be detected precisely, which offers a variety of further applications of the device, such as monitoring barrier tissue integrity with high temporal resolution.<sup>[27]</sup>

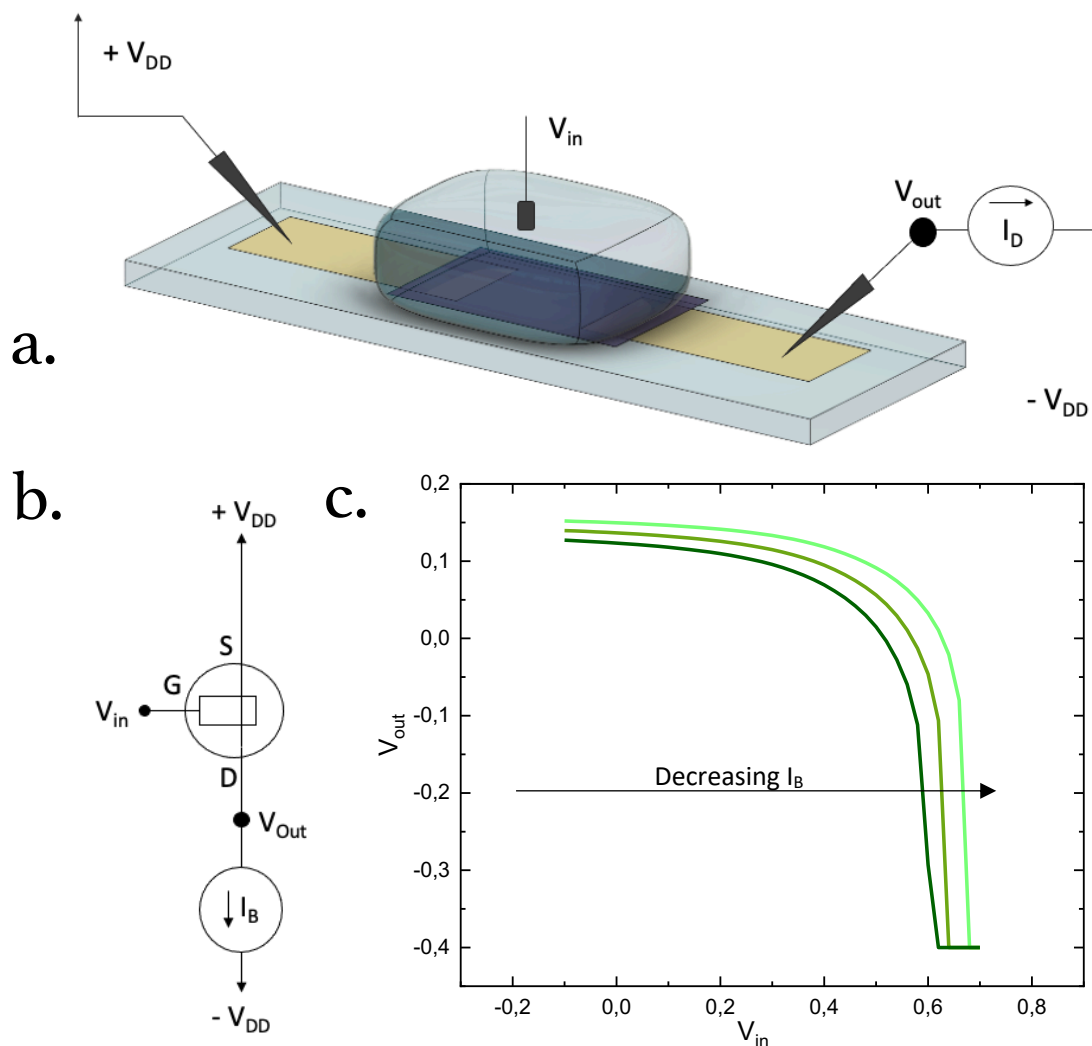


**Figure 4: Device architecture in the current-driven configuration and corresponding electrical characteristics.**

a) Current-Driven OECT configuration, with  $V_{in}$  applied at the gate and  $V_{out}$ , set by  $V_{DD}$ , measured at the drain. b) Electrical circuit of the current-driven configuration. c) Typical transfer characteristics of the OECT in the current-driven configuration with varying current bias  $I_B$ , the curves undergo a shift to higher  $V_{in}$  with decreasing current bias  $I_B$ .

An important classification in this context is the switching voltage  $V_{SW}$ , extracted from the graph (Fig.8c) as  $V_{in}$  at  $V_{out} = V_{DD} / 2$  and can be calculated as followed:

$$V_{SW} = V_{DD} + qp_0C_V^{-1} - (I_B/\beta)^{1/2} \quad (2)$$

$$\beta = W\mu C_V t(2L)^{-1} \quad (3)$$

Where  $q$  is the elementary charge,  $p_0$  is the density and  $C_V^{-1}$  the volumetric capacitance of PEDOT:PSS. The current prefactor  $\beta$  gives information about the dimensions of the channel volume, such as width  $W$ , length  $L$ , thickness  $t$ , and the charge carrier mobility  $\mu$  as well as the volumetric capacitance  $C$ .<sup>[33]</sup> As figure of merit  $V_{SW}$  can be extracted easily from the  $(V_{out}-V_{in})$ -transfer characteristics (**Fig.8c**), it allows simple and quick quantification of measurements.

The OECT in the current-driven configuration is emphasized to be a useful tool for approaches, such as cell barrier assessment, since it provides high sensitivity at low voltages and an easy evaluation of results. It is specifically these properties that are also exploited in this work to monitor the integrity of various epithelial barrier tissues. By integrating a barrier tissue into the device setup, in between gate and channel, ion transport into the channel is impeded, a higher  $V_{in}$  is needed to dedope the channel and the  $(V_{out}-V_{in})$ -transfer characteristic experiences a right shift. This phenomenon leads to the assumption that barriers with various levels of impedance, cause varying electrical response of the OECT. Since the OECT in the current-driven configuration is highly sensitive, the smallest shift in  $(V_{out} - V_{in})$ -transfer characteristics can be observed, which is highly desirable for biological application.

## 1.4 Epithelial Cells and Cell Junctions

In the 1830s Theodor Schwann proposed his theory, that all organisms are composed of one or more cells and that the cell is the structural unit of life.<sup>[36]</sup> Today, it is well known, that as a biological organization unit, cells play an indispensable role for living organisms. The basic properties of a cell are a functional metabolism, complexity, organization, ability to respond to stimuli, self-regulation, and carrying out mechanical activities.<sup>[37]</sup>

Eukaryotic vertebrate cells contain membrane-bound organelles such as mitochondria and endoplasmic reticulum, but also functional molecules, like proteins and nucleic acids, forming the DNA. The cell organelles are surrounded by a fluid, the cytosol. The entirety of the internal space of the cell is called cytoplasm, whereby a phospholipid bilayer separates the cytoplasm from the extracellular space.<sup>[38]</sup> Most eukaryotic cells form multicellular organisms with a common metabolism, whereby specific cell types take over certain functions, such as respiration, digestion, and barrier functions to organs. In such organisms, cells with similar structures are aggregated to tissues, performing specific functions.<sup>[38,39,40]</sup> Vertebrate tissues can be organized in four different types: connective, muscle, nervous, and epithelial tissue.<sup>[41]</sup>

Epithelial tissues cover the internal and external surfaces of the body, e.g. the epidermal covering of skin and the outlining of the respiratory and gastrointestinal tract.<sup>[42]</sup> The cells are tightly connected

via protein complexes and create a semipermeable, physical barrier to separate organs from external milieu.<sup>[42,43]</sup> In this way epithelia creates the biggest obstacle for ions and small molecules to reach target organs and the blood stream, and makes it impossible for “invaders” to pass this protective barrier.<sup>[27]</sup> Still there are several transport routes, that ensure essential nutrients to reach the blood stream, whereby a distinction is made between transcellular transport, across the cell lumen, and paracellular transport, in between two adjacent cells.<sup>[27,44]</sup>

Epithelial cells can be divided into an apical, lateral and basal cell membrane (**Fig.5**), defining a certain polarity.<sup>[42]</sup> The apical end of these cells has protrusions, that facilitate absorption of nutrients and is usually directed away from the cell lumen.<sup>[42,36]</sup> The lateral membrane constitutes the contact point between adjacent cells and contains various protein complexes that establish cell-cell contact. To anchor the cells to the underlying connective tissue, the basal membrane forms cell-matrix contacts to the basal lamina of the connective tissue.<sup>[38,42]</sup>

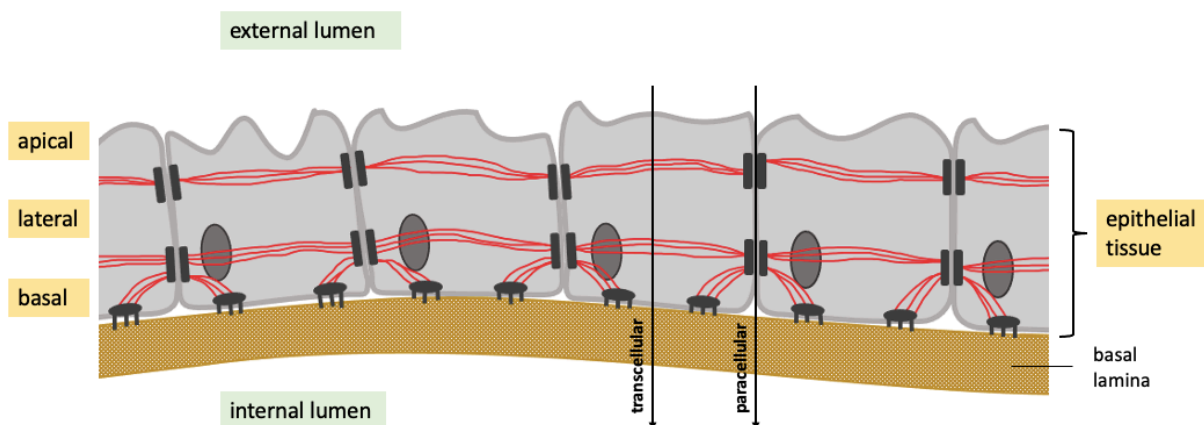


**Figure 5: Schematic illustration of epithelial tissue anchored to the extracellular matrix.**

Epithelial cells are connected to each other via junctional protein complexes and anchored to a thin layer of extracellular matrix tissue via cell-matrix contacts. Adherent junctions as well as desmosomes link the cytoskeleton of adjacent cells and maintain tissue stability in this way. Cell-matrix contacts are also anchored to the cell via cytoskeleton structures.

Regarding the property of epithelial cell layers as barriers, especially the cell-cell-junctions in between the cells are of great importance. A closer view on the intercellular space, reveals four types of junctional complexes: tight junctions, adherent junctions, desmosomes, and gap junctions.<sup>[36,42]</sup> Adherent junctions and desmosomes belong to the types of anchoring junctions, linking the cytoskeleton of adjacent cells (**Fig.5**) to maintain tissue stability, whereby adherent junctions are more likely to occur towards apical membrane and desmosomes towards the basal membrane. Gap junctions are communication linkages, that enable the exchange of molecules between two cells and are located towards the basal membrane.<sup>[38,42,43]</sup> In contrast, tight junctions (TJs) seal the intracellular space between adjacent cells, thus, are crucial for separation of external lumen and basal lamina in confluent cell layers and barrier tissues. TJs fulfill two main functions, they regulate the paracellular

exchange of ions and molecules between an internal and external lumen. By opening, they allow the internal space to absorb water and nutrients, but prevent toxins and pathogens to cross the epithelial barrier into the blood, which is referred to as gate property. Second, they act as a fence, preventing apical and basal membrane proteins migrating to the other side, thus, maintaining cell polarity.<sup>[43,45,46]</sup> In recent years, more discoveries about TJs and their structure, function and regulation were made, but the precise mechanism of opening and closing remains unclear. It is certain, that TJs dynamically regulate the permeability of the paracellular pathway in response to external stimuli. Looking at TJs in more detail, shows a number of protein complexes, such as transmembrane protein complexes, including various claudin and occludin derivatives, tricellulin and JAM, spanning the intercellular space and mediate cell-cell adhesions. On the other hand, a large number of peripheral cytoplasmic proteins are associated with these transmembrane proteins (**Fig.6**).<sup>[47,48]</sup> The latter consists of scaffold proteins, e.g. zonulin (ZO-1, ZO-2, ZO-3), which anchors the transmembrane junctions to the actin cytoskeleton and are involved in the recruitment of regulatory proteins, such as kinases, G-proteins, and nuclear transcription factors. In this way, zonulin interacts with specific apical surface receptors, leading to polymerization of actin microfilaments and subsequent TJ disassembly.<sup>[49]</sup> The upper located integral TJ proteins are claudins, determining charge and size selectivity of the paracellular transport and maintain cell polarity. Occludin also contributes to gate and fence functions, representing the key regulator of paracellular seals, besides claudins, while tricellulin and JAM are involved in adhesion between adjacent epithelial cells and contribute to the fence function of epithelia.<sup>[48]</sup>

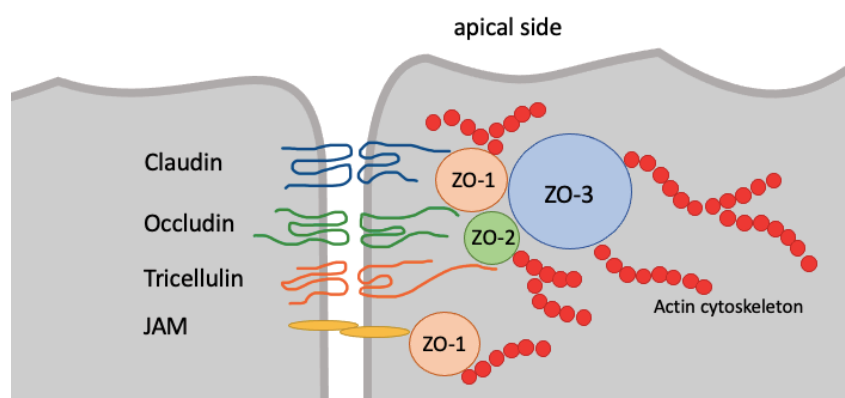


**Figure 6: Schematic illustration of tight junction proteins**

Tight junctional proteins occur near the apical side of epithelial cells. Claudin, occludin, tricellulin and JAM are transmembrane proteins and located in the phospholipid bilayer in between two adjacent cells. Whereas zonulins (ZO-1, ZO-2, ZO-3) are located in the cytoplasm of the cells.

Tightness and quantity of TJs in epithelia alters according to the respective purpose of each tissue.<sup>[44]</sup> The tightest barrier tissues are the blood-brain-barrier and the skin epithelium. Taking the example of the gastrointestinal tract, epithelia can be classified in leaky (small intestine), intermediate tightness

(colon) and tight (esophagus). The tightness of an epithelial tissue can be quantified by the parameter transepithelial electrical resistance (TEER), reflecting the paracellular ion flow. Common techniques for barrier tissue integrity assessment are the TEER measurement<sup>[50]</sup> with a handheld EVOM volt-ohmmeter or the cellZscope.<sup>[51]</sup> Both techniques rely on two electrode configurations, where low frequency signals are difficult to obtain for tight cell layers, due to low current.<sup>[52]</sup> Biological established methods to monitor living cells, such as immunofluorescence staining, suffer from inaccuracy, are time-consuming and invasive, forbidding *in vivo* application.<sup>[53]</sup> In this context, the OECT offers a sensitive, at low voltages operating, label-free electrical measurement and, thereby, fulfills the most essential requirements to monitor living cells non-invasive and be established as a promising state-of-the-art biosensor.<sup>[43,48]</sup>

In this work, the field of drug delivery is introduced as an application for the OECT as dynamic biosensor. Regarding common drug delivery research, the gastrointestinal tract is mainly used as model for oral drug absorption, whilst many clinically approved drugs are not absorbable over, e.g., skin epithelia, particularly because of the tight epithelia. Some drugs pass the epithelial layer by transcellular pathway, but especially the absorption of hydrophilic substances is governed by the intercellular junctions, triggering the need of novel drug delivery systems.<sup>[47,48,54]</sup> The discovery of TJ structures (**Fig.6**), already led to more understanding in the functionality of barrier tissues and to the development of so-called tight junction modulators (TJ modulators), targeting these specific structures. TJ modulators are able to modify the tight junctions and the paracellular permeability of various epithelia, including the blood-brain-barrier, skin, gastrointestinal tract and airway epithelium, each representing a major barrier for drug delivery.<sup>[27,48]</sup> TJ modulators of the last generation suffer from unspecific and uncontrolled modulation, and an effective dose close to toxicity, whereby new generation TJ modulators can be potentially used to reversibly open TJs, to temporary increase paracellular transport and allow drug delivery to the systemic circulation or to specific target organs, which is the long-time goal in biomedical research.<sup>[27,35,48]</sup>

Here, Ethylenediaminetetraacetic acid (EDTA) is introduced as a TJ modulator. EDTA is extensively used as chelator of divalent cations, such as  $\text{Ca}^{2+}$ . Nowadays, EDTA has already found many applications in medical treatment, such as poisoning treatment, regulating calcium deposit in eyes or removing copper in patients with the genetic Wilson's disease.<sup>[55]</sup> But chelating agents generally also seem as promising candidates in the field of drug delivery. It was already in 2002 that B. Rothen-Rutishauser et al. presented the disassembly and reassembly of TJs after exposure and removal of a calcium chelating agent.<sup>[56]</sup> They introduced the calcium-dependent transmembrane protein cadherin as the initial organizer of TJs and explain the disassembly of TJs after extracellular calcium chelation by that.<sup>[56,57]</sup> The mechanism that underlies the TJ modulation was examined in more detail by Scherrine Tria et. al in 2012.<sup>[58]</sup> Accordingly, cadherins are sensitive to extracellular calcium. In absence of calcium,

cadherins are not able to form hetero- or homojunctions between adjacent cells, TJs are internalized and paracellular permeability increases. Further TJ associated proteins that are calcium-dependent are G proteins, kinases and calmodulin, promoting TJ disassembly in response to calcium absence. However, information about TJ dynamics are still scarce and need further investigation, triggering the need of novel investigation techniques for pharmaceutical research





## 2. Motivation and Outline

Controlling the barrier function of epithelial barrier tissues is of great importance for drug development and pharmaceutical research. The manipulation of a barrier tissue is applicable in targeted drug delivery, which is of particular interest for drug delivery across tight barriers, such as the skin, blood-brain-barrier, and some parts of the gastrointestinal tract. Such drug delivery assays require models to assess effects of the toxicity and efficacy of drugs. An efficient method to monitor the manipulation of barrier tissues will ensure better understanding of TJ dynamics and to apply this knowledge in drug testing, aiming for replacement of animal studies for safety assessment and toxicological profiling.<sup>[27,58]</sup> Here, the OECT in the current-driven configuration is demonstrated as a useful tool to assess dynamic changes in TJs, which is relevant for targeted drug delivery. In comparison to other techniques, such as immunofluorescence and permeability assays, transepithelial electrical (TEER), and electrochemical impedance spectroscopy (EIS) measurements, the non-invasive OECT outstands offering high local and temporal resolution together with reproducibility and the possibility for dynamical *in-vitro* studies, allowing strongly enhanced sensitive monitoring of cell barrier integrity. To assess circuit parameters selectively for all compounds of the OECT with integrated barrier tissue, electrochemical impedance spectroscopy (EIS) is performed. Gaining insights in the working principle of an OECT with integrated barrier tissue, the transient response of the OECT is investigated for barriers of varying impedances. The experiment is performed with the OECT in standard and current-driven configuration, whereby the latter one is further examined for different scan rates. Furthermore, the OECT is applied as a dynamic biosensor investigating the response of barrier tissue from two different epithelial cell lines to the tight junction modulator EDTA. Monitoring barrier tissue modulation *in situ* is important to quantify the effect of TJ modulators on barrier tissues and eventual permanent barrier disruption and to analyze TJ modulators, such as EDTA, as possible candidates for drug delivery systems.. The results are validated with TEER measurements.

Transient response experiments as well as tight junction modulation were performed with the Madin-Darby Canine Kidney II (MDCKII) and the colon carcinoma (CaCo-2) cell line, as *in-vitro* kidney and colon model, respectively. Both of the cell lines are found in the small intestine and are examples for intermediate cell barriers, whereby MDCKII cells reach a TEER value of  $\sim 100 \Omega\text{cm}^2$ <sup>[59]</sup> and CaCo-2 cells can reach  $\sim 400 \Omega\text{cm}^2$ .<sup>[60]</sup>

In this work, the operation of an OECT with an implemented barrier tissue is investigated, focusing on the transient response. Further, the OECT with integrated barrier tissue is used to sense tight junction modulation dynamically. The results prove the suitability of OECT technology towards *in-vitro* monitoring of reversible TJ modulation, which offers valuable information's for drug delivery applications.



### 3.Experimental

This chapter lists the material used for the research work, as well as an explanation of device fabrication, characterization methods and cell preparation for biological applications. The fabrication of organic electrochemical transistors was carried out in sterile atmosphere and is outlined in detail. Cell preparation includes the culturing of different cell lines and further preparation for biological experiments. The experimental section completes with a listing of characterization methods to analyze the device and the cell layer.

#### 3.1 Material

##### Chemicals

<b>PEDOT:PSS (Clevios PH 1000)</b>	Heraeus, Hanau, GER
<b>Ethylene glycol</b>	Serva, Heidelberg, GER
<b>DBSA</b>	DuPont, Neu-Isenburg, GER
<b>GOPS</b>	Sigma-Aldrich, Taufkirchen, GER
<b>Soap (Micro90)</b>	IPC, London, UK
<b>EMEM</b>	Lonza, Walkersville, USA
<b>PBS</b>	Lonza, Walkersville, USA
<b>FBS</b>	Invitrogen, Karlsruhe, GER
<b>Glutamine (GlutaMax-1)</b>	Invitrogen, Karlsruhe, GER
<b>Penicillin &amp; Streptomycin (PenStrep)</b>	Invitrogen, Karlsruhe, GER.
<b>Trypsin/EDTA</b>	Gibco, Paisley, USA
<b>Trypan Blue</b>	Sigma Aldrich, Taufkirchen, GER
<b>Collagen</b>	Sigma-Aldrich, Taufkirchen, GER
<b>PFA</b>	Sigma-Aldrich, Taufkirchen, GER
<b>Triton X-1000</b>	Sigma-Aldrich, Taufkirchen, GER
<b>BSA</b>	Sigma-Aldrich, Taufkirchen, GER
<b>Sylgard 184</b>	Dow Corning, Michigan, USA
<b>Curing Agent</b>	Dow Corning, Michigan, USA
<b>EDTA</b>	Serva, Heidelberg, GER
<b>DRAQ5</b>	Biostatus Leicestershire, UK,

## Consumables

<b>Counting slides</b>	Biorad, Hercules, USA
<b>12mm Transwells</b>	Corning Incorporated, Kennebunk ME, USA
<b>12-well culturing plates</b>	Corning incorporated, Kennebunk ME, USA
<b>8-well culturing slide</b>	IbidiTreat, Gräfelfing, GER
<b>Pipette tips</b>	Eppendorf AG, Hamburg, GER
<b>Eppendorf tubes</b>	Eppendorf AG, Hamburg, GER
<b>Falcon tubes (15ml, 50ml)</b>	Greiner AG, Kremsmünster, Austria
<b>Syringe (5ml, 10ml)</b>	B.Braun AG, Melsungen, GER
<b>Needle</b>	B.Braun AG, Melsungen, GER
<b>Filter (0,45 <math>\mu</math>m)</b>	Merck Millipore Ltd., Darmstadt, GER

## Antibodies

**Table 1:** List of Antibodies

<b>Antibody</b>	<b>Host</b>	<b>Clonality</b>	<b>Company</b>
FITC488 conjugated anti zonulin1 IgG	Mouse	monoclonal	Invitrogen, Karlsruhe, GER
Alexa594 conjugated anti occludin IgG	Mouse	monoclonal	LifeTechSci, Shenzhen, China

## Cell lines

**Table 2:** List of Cell lines

<b>Cell line</b>	<b>Cell type</b>	<b>Company</b>
CaCo2	Colorectal adenocarcinoma - epithelial	DSMZ, Braunschweig, GER
MDCKII	Canine Kidney- epithelial	DSMZ, Braunschweig, GER

## 3.2 Methods

### 3.2.1 Device Fabrication of Organic Electrochemical Transistors

In the following section, the fabrication of OECT's is described. All processes occur in the cleanroom under particle free conditions, if not stated differently, to avoid contamination.<sup>[17]</sup> The device consists of a 3 cm x 3 cm borosilicate glass substrate (EAGLE XG) and an array of three 0.2 cm x 1 cm gold electrode pairs, with an adhesive chromium layer underneath, connected via the conductive PEDOT:PSS channel (**Fig.7**).

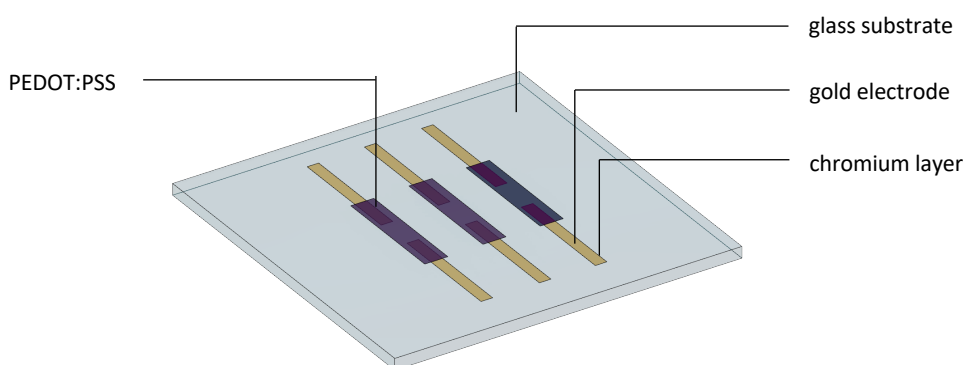


**Figure 7: Schematic illustration of the fabricated device sample.**

Sample, consisting out of a square glass with an array of three transistors. Each transistor incorporates two gold electrodes with an adhesive chromium layer underneath. The electrodes are connected via the conductive polymer PEDOT:PSS.

The PEDOT:PSS formulation consists of PEDOT:PSS to which GOPS, DBSA and ethylene glycol were added. PEDOT:PSS (95 vol.%) solution was mixed with ethylene glycol (5 vol.%), 1-2 drops of surfactant DBSA, and GOPS in a ratio of 1:1000. The polymeric dispersion was stirred for at least 1 h before further use, with an roll shaker (IKA® ROLLER 6 Mixer).

To avoid contaminations and improve device performance, the glass substrates were cleaned before further processing. The substrates were sonicated with a 1:20 (vol/vol) soap solution in DI-water in a UV-bath (Fisherbrand®) for 15 min. To remove soap and aqueous soluble residues, the substrates were flushed with deionized water and dried with nitrogen (airforce gun). The substrates were sonicated (Fisherbrand®) in a 1:1 (vol/vol) solvent mixture (Acetone/Propanol), removing organic residues. The substrates were dried at 140 °C for 10 min. A further UV-ozone cleaning, using the UV-ozone-oven (UVOCS®) for 20 min, removes remained particles and activates the glass surface.

Metal evaporation was performed in a glove box, under exclusion of air and moisture, in an inert nitrogen atmosphere. The adhesive chromium layer (5 nm) as well as source and drain contacts (100 nm) were thermally evaporated (Vactec BV), using a shadow mask to define the active area. Arrays of three electrode pairs were patterned on each glass substrate. After a 20 min UV-ozone

treatment, the PEDOT:PSS dispersion was filtered through a 0,45  $\mu\text{m}$  filter and spin-coated (SÜSS MicroTec) onto the substrate. To reach a layer thickness of around 300 nm, the following recipe was used for film deposition: 3 layers at 1500 rpm, 650 rpm and 650 rpm, for each 30 s. In between each layer, the PEDOT:PSS channel was patterned with a wet cotton tip, resulting in an active area of 2 mm width, 1 mm length, and 300 nm height between gold source and drain electrodes. Samples were undergoing a 1 min soft bake on a hot plate, in between spin coating steps and kept at 140°C in the oven over 1 h, after last round of spin-coating. The samples were bathed in deionized water over night, for swelling of the active area and dried with nitrogen (airforce gun) the next day. Before further use, a poly(methyl methacrylate) (PMMA) – well was placed on top of the device, using double-sided tape to prevent leakage. The PMMA well confines the electrolyte and defines a curtain volume.

### 3.2.2 Cell Preparation

Handling with the cells was carried out exclusively in sterile environment such as laminar flow benches and an incubator as sterile storage space. Objects and chemicals that were brought under the laminar flow bench must be sterilized with ethanol before.

#### 3.2.2.1 Cell Culturing of CaCo2 and MDCK II Cells

In this work, CaCo-2 and MDCKII cell types were used. As cell culture medium, Eagle's Minimum Essential Medium (EMEM) was used for both cell types. EMEM was supplemented with fetal bovine serum (FBS) (10 vol%), Glutamine (1 vol.%) and Penicillin/Streptomycin (PenStrep) (1 vol%). To avoid any kind of contamination, FBS and Glutamine were sterile filtrated before added to the medium.

To bring kryo frozen cells into culture, the frozen vial was thawed manually and transferred into a 15 mL vial. 9 mL Eagle's Minimum Essential Medium (EMEM) was added to the cells, resulting in ~10 mL cell suspension. After centrifugation at 500 g for 3 min, the separated suspension consisted, according to the density of its components, of a supernatant, which was discarded, and a cell pellet. The remained cell pellet was resuspended first in 2 mL EMEM, then dissolved in 15 mL EMEM and transferred into a cell culturing flask.

Once the cells were seeded, EMEM was exchanged every 2-3 days. The cells were splitted and passaged after reaching a confluency of approximately 80 %. For splitting, EMEM was discarded and the cells were exposed to 7.5 mL Trypsin/EDTA at 37 °C and 5 % CO<sub>2</sub> for 5 min for cell detachment. Further, 7.5 mL EMEM was added and the cell suspension was centrifugated at 150 g for 3 min. The supernatant was discarded, whereas the cell pellet was resuspended in 1 mL EMEM. The resuspension was repeated after adding 3 mL more.

For determining cell viability, the cell suspension was mixed with Trypan Blue in a 1:1 (vol/vol) ratio, living cells absorbed the colorant, and were detected by an automated cell counter (TC10, Bio-Rad).

For further cell culturing, 500.000 cells with an average live count of ~95 % / 4 mL were seeded in a cell culture flask, EMEM was added to a total volume of 15 mL.

For this study, the cells were seeded into 12-well filters (costar) (**Fig. 7**), located in a well plate. A total of 150.000 cells in 500  $\mu$ L was seeded in the apical compartment into each filter. The basal compartment was filled with 1.5 mL EMEM, so that inner and outer medium are on the same level, reducing osmotic pressure on the cell layer

### 3.2.2.2 Filter Preparation

Cell filters contain a semipermeable polycarbonate membrane with a pore size of 0.4  $\mu$ m and an area of 1.12 cm<sup>2</sup>. The surface of each cell filter was reduced by 90 %, to ~ 0.08 cm<sup>2</sup>, in order to enhance the resistance of the active area. Therefore, polydimethylsiloxane (PDMS) was coated on the back side of the filters (**Fig.7**). The modified filters were cured for 48 h at room temperature (~ 25 °C). Under the laminar flow bench, the filters were sprayed with ethanol and put under a UV-lamp for at least 1 h. After the UV-sterilization, the filters were coated with 100  $\mu$ l collagen to enhance adhesion of cell layers. The collagen coated filters were incubated over night at 37 °C and 5 % CO<sub>2</sub> atmosphere. After, the collagen was removed and the filters sterilized under an UV-lamp for further 2 h and dried for another 2 h under the laminar flow bench.



**Figure 8: Filter preparation**

a) apical side of the plane filter. b) basal side of the plane filter. c) basal side after applying PDMS, leading to a decreased measurement area.

#### 3.2.2.2.1 PDMS Preparation

To prepare PDMS, Sylgard 184 and the Curing Agent were mixed in a ratio of 1:10 (vol/vol), stirred well with an Eppendorf tip and centrifugated at 5000 rpm for 2 min. Before application, the silicone was heated at 200 °C with a heat gun until the viscosity decreased, which provides an easier application of PDMS onto the filter.

### 3.2.3 Impedance Spectroscopy for Cell Layer Characterization

Electrochemical Impedance Spectroscopy determines the impedance of electrochemical systems such as the OECT, as a function of the frequency of an AC voltage.<sup>[61]</sup> The measurement was performed with a potentiostat (FRA2  $\mu$ Autolab Type III) in a three-electrode configuration. An alternating current (AC) was applied at different frequencies in the range of 0.001-10000 kHz to record potential difference between drain and source. EMEM was used as electrolyte for the OECT. Drain and source electrodes were shorted and used as the working electrode. A Platin (Pt) (Warner Instruments) as counter electrode and silver/silver chloride (Ag/AgCl) electrode (Warner Instruments) as a reference electrode were immersed into the electrolyte. To obtain capacitance and resistance values, the data was fitted with an equivalent R-C circuit and R-R/C -C circuit for the measurement with integrated barrier tissue.

### 3.2.4 OECT Operation

Electrical measurements with the OECT as operating system were performed in an incubator at 37 °C humidified atmosphere with 5 % CO<sub>2</sub>, and with EMEM as electrolyte to maintain cell culture conditions. For OECT measurements, a gate electrode (Ag/AgCl pellet, 2 mm, Warner Instruments) was immersed into the electrolyte. Source and drain electrodes were connected to the Keithley 4200-Semiconductor Characterization System via pins. During OECT measurements, the effective gate voltage was kept under 1 V at all time, to avoid water electrolysis and cell damage.<sup>[33]</sup> The data was analyzed by OriginLab software.

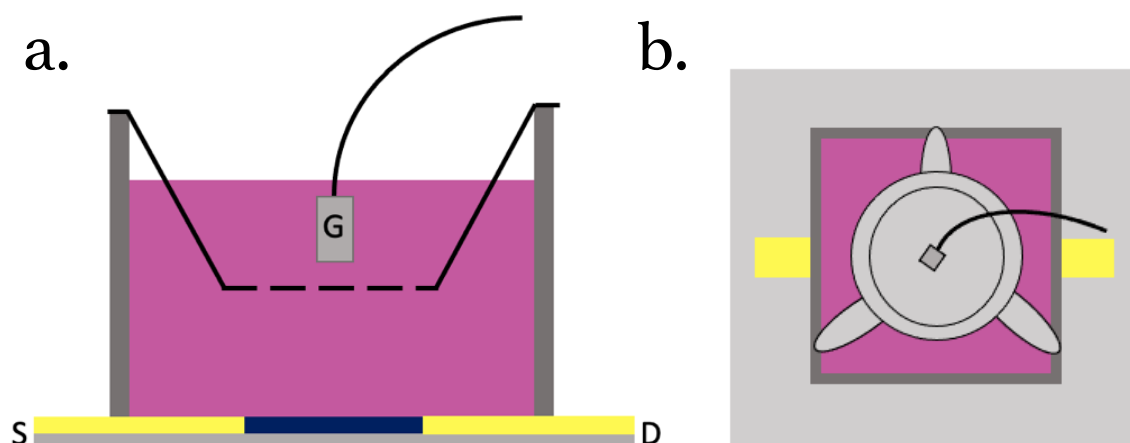


**Figure 9: device architecture of an organic electrochemical transistor with integrated filter.**

OECT device structure with a PMMA well glued on top of the electrodes. The PMMA well is filled with a volume of 1,5 ml EMEM, used as electrolyte. The filter includes 0,5 ml EMEM apical. The gate electrode is immersed into the electrolyte in the apical compartment. **a)** front view of OECT setup. **b)** top view of OECT setup.



### 3.2.4.1 Transfer Characteristics

Transfer characteristic measurement were performed before every experiment, to determine  $I_D$  of the device. For this measurement, the source is grounded,  $V_{DS} = V_D$ . Transfer characteristics were performed at certain  $V_D$  of (-0.1; -0.2; -0.3; -0.4) V, by sweeping  $V_G$  from [-0.2 V; .6 V] in 10 mV steps and a hold time of 2 s.

### 3.2.4.2 Transient Response measurement in standard OECT configuration

For transient response measurement of the OECT, source is grounded ( $V_{DS} = V_D$ ).  $V_D$  was kept at - 0.4 V and a  $V_G$  pulse of 0.5 V was applied for ~15.5 s. The corresponding  $I_G$  and  $I_D$  responses were measured and plotted against the time for further analyzation. To determine the effect of a barrier between gate electrode and channel, filters with different impedances were incorporated into the measurement setup.

### 3.2.4.3 Transient Response Measurement with the OECT in Current-Driven configuration

Transfer ( $V_{out} - V_{in}$ ) characteristics were measured with the OECT in the current-driven configuration, at  $V_{DD} = -0.2$  V ( $V_{SW} = 0.1$  V) and  $I_B = 4.5$  mA, for a  $V_G$  range from -1.5 V to +5.5 V, swept in 10 mV steps. The measurement was performed for different sweep delays (0; 0.5; 1; 1.5; 2; 5; 0) s at 2 s hold time. Transient response is determined for incorporated barriers of varying impedance.

### 3.2.5 Trans Epithelial Electrical Resistance Measurement of CaCo2 and MDCK II Cells

The TEER was measured in an EndOhm chamber, designed for 12-well filter. The filter in presence of a cell layer is then between the top electrode, attached to a cap, and the concentric bottom electrode of the chamber. Both electrodes incorporate a voltage sensing Ag/AgCl pellet in the center with a current sensing part around and were connected to a volt-ohm-meter (EVOM2, World Precision Instruments) via cables.<sup>[50]</sup> Once a cell layer is integrated into the setup, the top electrode was immersed in the apical compartment of the filter. A total volume of 2.5 ml EMEM, was added to the chamber, to reduce osmotic pressure for the cell layer.

To determine the TEER, an alternating current (AC) of 12.5 Hz was applied between the electrodes, flowing across the cell layer. The resulting current and voltage values were measured and adapting the Ohm's Law, the resistance can be calculated as the ratio of the measured voltage and current.<sup>[60,50,62]</sup>

### 3.2.6 Immunofluorescence Staining to Visualize Tight Junctional Proteins

CaCo2 and MDCKII cells were seeded into 8-well culturing slides and cultured for 14 days before further use. Immunofluorescence staining was conducted on the tight junctional proteins occludin and

zonulin. Furthermore, the nucleus and parts of the cytoskeleton were stained to determine the morphology of the cells and to point out the confluence of the cell layer.

The staining is preceded by a cell layer fixation. In this procedure, the cells were bathed in 4 % paraformaldehyde (PFA) in phosphate buffered salt solution (PBS) for 10 min at room temperature (RT). After discarding the PFA, 0.1 % Triton-X-100 and 1 % bovine serum albumin (BSA) in PBS were added to the fixed cells and incubated for 2 h at RT. Thereby, Triton-X-100 permeabilizes the cell membrane and BSA reduces unspecific binding of the antibodies. After washing with PBS, the cells were incubated with fluorochrome-labeled antibodies (**Tbl.2**), diluted in PBS with a ratio of 1:1000, at 4°C overnight. For nuclei staining, Draq5 is diluted in a ratio of 1:1000 in PBS and added to the cells 20 min before analysis. The stained cell layers were examined under a confocal laser scanning microscope (cLSM). Antibody incubation and the following analyzation was conducted in the dark to prevent bleaching of the fluorochromes.

### **3.2.7 Detecting Tight Junction Modulation with the OECT in the Current-Driven configuration**

Tight Junction Modulation measurements were performed with the OECT in the current-driven configuration. The experiments were performed 14 to 21 days after seeding MDCKII and CaCo-2 cells, corresponding to a TEER of  $\sim 5000 \Omega$  for CaCo-2 cells and  $\sim 1000 \Omega$  for MDCKII cells. The TEER was determined before and after experiment. Samples were kept in humidified atmosphere at 5 % CO<sub>2</sub> during the whole experiment.

To assure device stability, transfer characteristics ( $V_{out} - V_{in}$ ) were measured for 1.5h, with an integrated, PDMS coated filter. Then, the plane filter was replaced with a cell filter (MDCKII / CaCo-2) and  $V_{out} - V_{in}$  characteristics were measured for 2 h, to assure stable barrier functionality. Before the TJ modulator was added apical to the cell layer, the same volume of apical EMEM volume was removed to keep ionic concentration and osmotic pressure similar. In two experiments each, MDCKII and CaCo- 2 cells were exposed to 1mM and 10mM EDTA for 30 min. After treatment, the electrolyte was exchanged apical and basal, whereby a volume of 0.5 ml EMEM was kept basal for experiments with CaCo-2 cells. The measurement was continued overnight. To minimize parameter variations, the experiment was performed in a continuous measurement. To analyze cell barrier modification, the ( $V_{out} - V_{in}$ ) -transfer characteristic shift was quantified by  $V_{SW}$ .

10 mM – MDCKII measurement is performed at  $I_B=1.6$  mA, 1 mM – MDCKII measurement at  $I_B=2.5$  mA. A different OECT device was used for CaCo-2 measurements. Here,  $I_B = 3.5$  mA is applied for 10 mM experiment and  $I_B=3.3$  mA for 1 mM experiment.

## 4. Results and Discussion

### 4.1 Characterization of Barrier Tissue with Electrochemical Impedance Spectroscopy of the Organic Electrochemical Transistor

Electrochemical Impedance Spectroscopy was performed to obtain characterizing circuit parameters selectively for all compounds in the electronic circuit of an OECT with integrated barrier tissue. The measurement was performed for the device only, an integrated plain filter, an integrated filter of reduced area (PDMS-coated), and with barrier tissue of the cell lines MDCKII and CaCo-2 seeded on a filter of reduced area. The data was fitted with an equivalent circuit, to selectively determine resistance and capacitance contributions of the total impedance spectrum to the respective system compound.

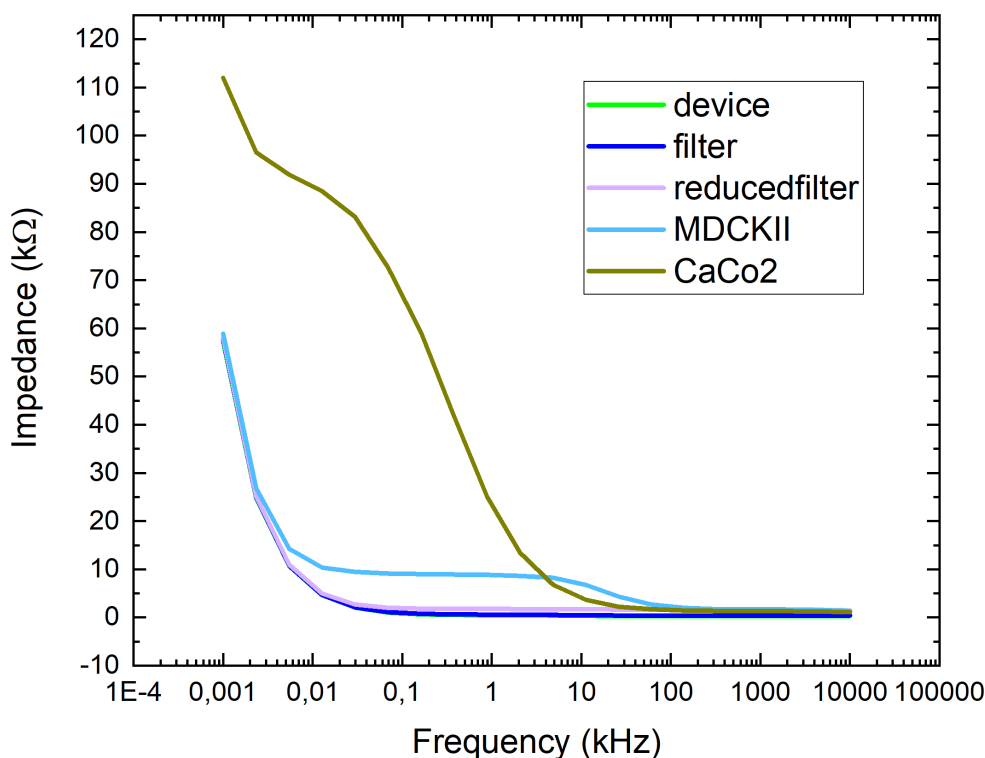


**Figure 10: Electrochemical Impedance Spectra of barriers of varying impedance**

EIS measurements are performed for the device only, an integrated plain filter, an integrated filter of reduced area (PDMS-coated), and barrier tissue of the cell lines MDCKII and CaCo-2. The experimental data points are fitted to an RC circuit for device and filters and R-RC-C equivalent circuit, when integrating barrier tissues. To obtain resistance and capacitance contributions of each barrier, the impedance was measured in a frequency range from 0.001 to 10000 kHz

It is already known from literature that the electrolyte can be well modelled by an ohmic resistance  $R_{EL}$ , which dominates the total impedance at higher frequencies<sup>[63]</sup> and that the OECTs channel is capacitive  $C_V$ , dominating at lower frequencies.<sup>[11,64]</sup> From the electrochemical impedance (EI) spectrum for the device only, this frequency-dependence can be obtained. Here, the graph displays a linear decline at lower frequencies, representing  $C_V$ , until  $R_{EL}$  is dominating, resulting in a flat line, if no

other components are included. The impedance spectrum for the device only and an integrated plane filter overlap and the curve for an integrated filter of reduced area is of higher resistance, indicating that not only the electrolyte resistance  $R_{EL}$  contributes to the total resistance of the system but also the resistance of the respective filter. In contrast, a major difference to the curves of both barrier tissues can be noticed, whereby the CaCo-2 barrier tissue offers the highest impedance of all measured systems. Furthermore, the curves for the barrier tissues show a plateau, which cannot be obtained for the curves without integrated barrier tissues. The barrier tissues have an impedance, composed of the resistance TEER and a capacitance  $C_{MEM}$ , contributing predominantly at mid-range frequencies between 0.01 and 100 Hz, leading to the formation of a plateau (**Fig.10b**).<sup>[51]</sup> This special characteristic allows a separation of the parameters of the barrier tissues from the peripheral impedances, dominating at lower and higher frequencies. The resistances in the system determine the height of the curves and the capacitance the slope, leading to the assumption that CaCo-2 barrier tissue must have a higher TEER and  $C_{MEM}$  than the MDCKII barrier tissue plateau. This phenomenon is representative for the barrier functionality of the barrier tissues and can be exploited to, e.g. study the behavior of the OECT in the presence of different barrier tissues.

The capacitance of the channel  $C_V$  seems to be the same for each system, whereby it is difficult to make a claim about  $C_V$  for measurement with the CaCo-2 barrier tissue, since the plateau is very high and not overlapping with the other curves. In order to find out more about the concrete resistance and capacitance values, an equivalent R-R/C-C circuit (**Fig.11b**) is applied.

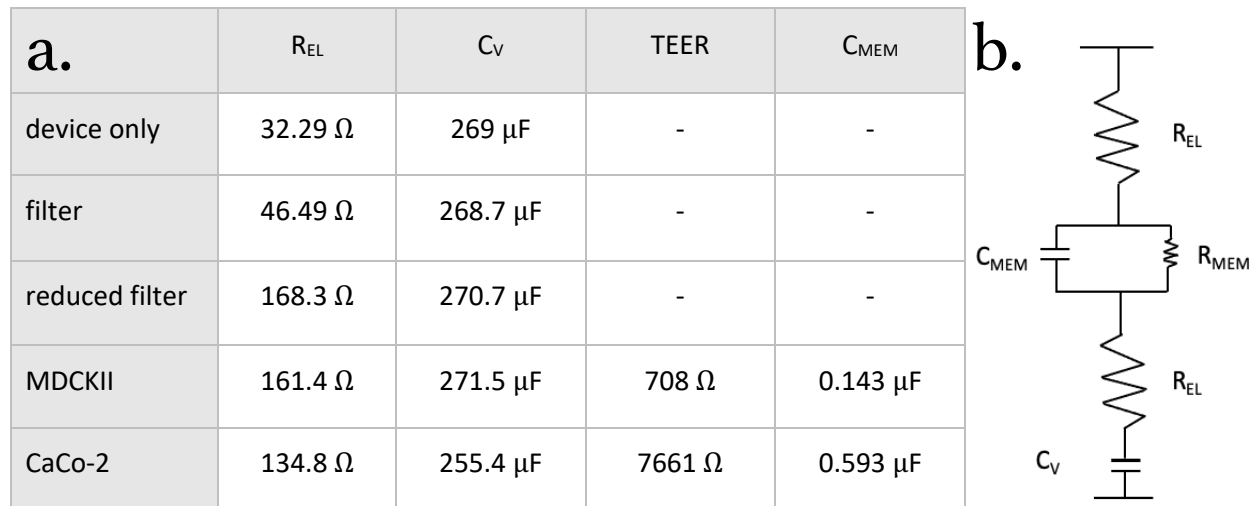


**Figure 11: Overview of capacitance and resistance values contributing to the total impedance and equivalent circuit.**

a) The table shows the separated values for impedance determining parameters in the utilized system. b) The equivalent electrical circuit that was applied to extract the values from a) is displayed. It shows the series arrangement of  $R_{EL}$  to parallel connected TEER and  $C_{MEM}$ , to  $R_{EL}$  and  $C_V$  in series.

By fitting the curves from **Fig.10** with the equivalent circuit, the impedance determining values are successfully separated. From **Fig.11a** it is confirmed that the CaCo-2 barrier tissue has , with 7661  $\Omega$ , a

significant higher TEER value than the MDCKII barrier tissue with  $708 \Omega$ , which is consistent with literature.<sup>[59,60]</sup> Further, the resistance of the barrier tissue is dominating over  $C_{MEM}$  being sufficiently low, such that  $C_{MEM}$  is negligible for following experiments.  $R_{EL}$  differs for the different integrated systems, which is related to the increased resistance of integrated filter of reduced area. The capacitance of the channel  $C_V$  does not change considerably, as the barrier tissue integrity does not affect the channel capacitance. The slight decrease for measurements with the integrated CaCo-2 barrier tissue is considered as an artefact.  $R_{EL}$  is slightly decreased for MDCKII- and CaCo-2 barrier tissues, compared to the integrated filter of reduced area. Since barrier tissue cells are seeded on top of filter of reduced area. This deviation is most likely due to the fact that the filter of reduced area are manually coated with PDMS and the area might vary for the different integrated filter, as the difference between filter of reduced area, MDCKII-, and CaCo-2 barrier tissues is not significant.

In conclusion, the barrier tissues could successfully be characterized quantifying electronic circuit parameter contributions. Further, the extracted information of resistance and capacitance contributions of the barrier tissue integrated in an OECT are important for the following experiments, to investigate the OECT as a biosensor for barrier tissues.

## 4.2 Investigating the Transient Characteristics of an Organic Electrochemical Transistor with an integrated Barrier Tissue

In this chapter, the transient response of the OECT in the standard and current-driven configuration is investigated. The measurement in standard configuration serves for analyzing of the electronic and ionic current in the system with different integrated barrier tissues. Further, the influence of a changing scan rate on the current-driven OECT is examined. As before, the OECT response to different barrier tissues is also investigated for the OECT in the current-driven configuration

### 4.2.1 Probing Transient Response Measurements in Standard Organic Electrochemical Transistor Configuration with a specific scan rate

Transfer characteristics in the standard configuration are performed at a single voltage step,  $V_G=0.5$  V. Electronic currents  $I_D$  and  $I_G$  are analyzed, whereby  $I_D$  (Fig.12) represents cation movement into the channel and  $I_G$  resembles the ionic current of anions (Fig.13). The measurement is performed for the device only, an integrated plane filter, a filter of reduced size and barrier tissues of CaCo-2 and MDCKII cell lines.

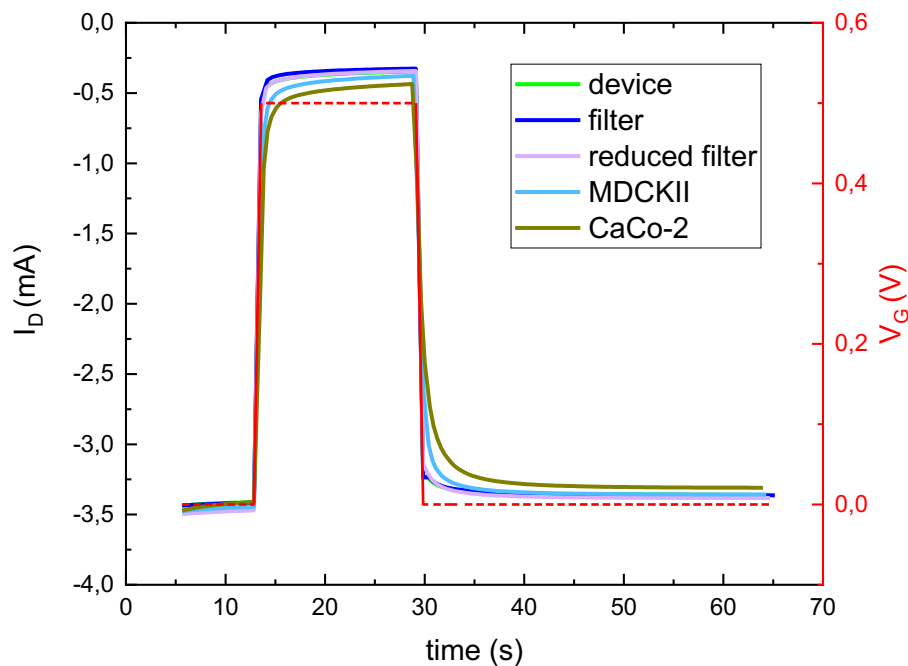


**Figure 12: Transient response of the electronic current with the OECT in the standard configuration.**

Measured drain currents  $I_D$  with the OECT in the standard configuration for integrated barriers with varying resistances and a  $V_G$  pulse of 0.5 V. Measurements are performed at a constant  $V_D$  of -0.4 V and for the device only, an integrated plane filter, a reduced (PDMS-coated) filter and MDCKII- and CaCo-2 barrier tissues.

The steady-state current is constant as a function of time, equals to  $I_D \sim -3.5$  mA before the  $V_G$  pulse is applied. In this state,  $I_D$  depends on the conductivity of PEDOT:PSS and the device geometry. Upon an

applied positive  $V_G$ , the gate electrode and the channel charge capacitively,  $I_D$  lowers exponentially to  $\sim -0.5$  mA, the transistor is in OFF-state. Once, the voltage pulse stops,  $I_D$  increases until initial value is reached, the transistor is in ON-state (**Fig.12**). When the  $V_G$  is applied, the amount of permeated cations from the electrolyte in the channel first exponentially increases and then gradually lowers until the channel is saturated and  $I_D$  remains constant. Upon removal of the voltage pulse, a recovery of  $I_D$  raises exponentially again, as cations drift out of the channel back into the electrolyte and then flattens out until the initial doping state is reached.

Further, it can be observed that the measurement for the device only and plane filter have the highest  $I_D$  response and reach ON-state the fastest. Cationic response with an integrated CaCo-2 barrier tissue is decreased, compared to the barriers with lower resistance and reaches ON-state later. This observation becomes reasonable when considering that barriers with higher resistance impede the passage of ions into the channel, thus, less cations reach the channel in the same time as for barriers with low impedances, leading to less dedoping and a more negative  $I_D$  value. Considering  $I_D$  recovery, ON-state is reached faster for measurements with barriers of low resistance, since cation flux is not impeded by a barrier.

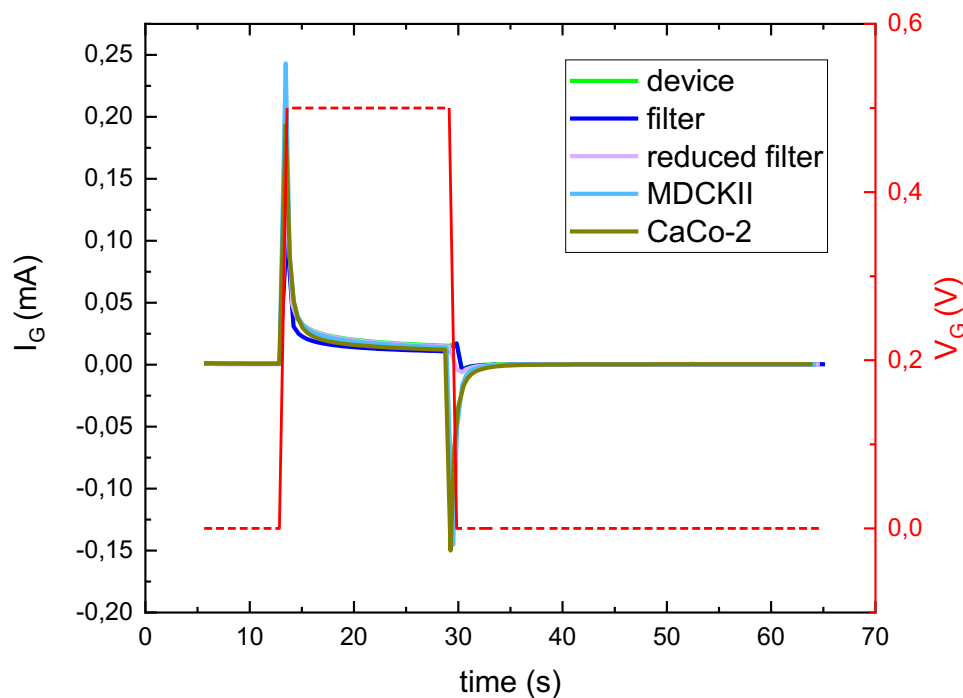


**Figure 13: Transient response of the ionic current with the OECT in the standard configuration**

Measured ionic currents  $I_G$  with the OECT in the standard configuration for integrated barriers with varying impedances and a  $V_G$  pulse of 0.5 V. Measurement is performed at a constant  $V_D$  of -0.4 V.

The anionic current  $I_G$  equals 0 mA in steady-state condition. Looking at  $I_G$  response to an applied  $V_G$  pulse, a positive current spike is observed that decreases exponentially. The removal of  $V_G$  pulse results in a negative current spike that exponentially increases until initial 0 mA is reached (**Fig.13**). That

indicates a fast migration of anions from the electrolyte towards the gate electrode in response to the  $V_G$  pulse. Once the gate electrode is saturated with anions,  $I_G$  decreases until about  $\sim 0$  mA, meaning that after some time there is almost no anion flux across the electrolyte. When  $V_G$  pulse is removed, the spike of negative  $I_G$  demonstrates the anion flux into the bulk of electrolyte towards the channel. In stabilization, ion movement is balanced, resulting in an electrical readout of 0 mA.

The spikes in  $I_G$  does not follow any trend. The measurement with the device only results in the lowest spikes, whereby spikes are higher for integrated plain filter and integrated filter of reduced area. The positive spike reaches the highest value for an integrated MDCKII barrier tissue, while the negative spike is highest for CaCo-2 barrier tissue. Generally, less change in  $I_G$  with increasing resistance of integrated filter and barrier tissues was expected, but from the results (**Fig.13**) the contrary is observed.

When comparing electronic and ionic response, it becomes clear that  $I_G$  occurs significantly faster than  $I_D$ , indicating that transient current is dominated by de-doping PEDOT:PSS.<sup>[65]</sup>  $I_G$  generates a short, high peak in transfer characteristics, but the peak falls very quickly back to initial steady-state conditions and is rather negligible, as ions do not diffuse in the bulk of channel but to gate electrode, which has a smaller surface area. To further compare the transient response measured as  $I_D$  and  $I_G$  over time, diffusion of ions once the  $V_G$  pulse stopped, is examined more closely. For simplification,  $I_G$  is integrated and the charge density  $Q$  is plotted over time.

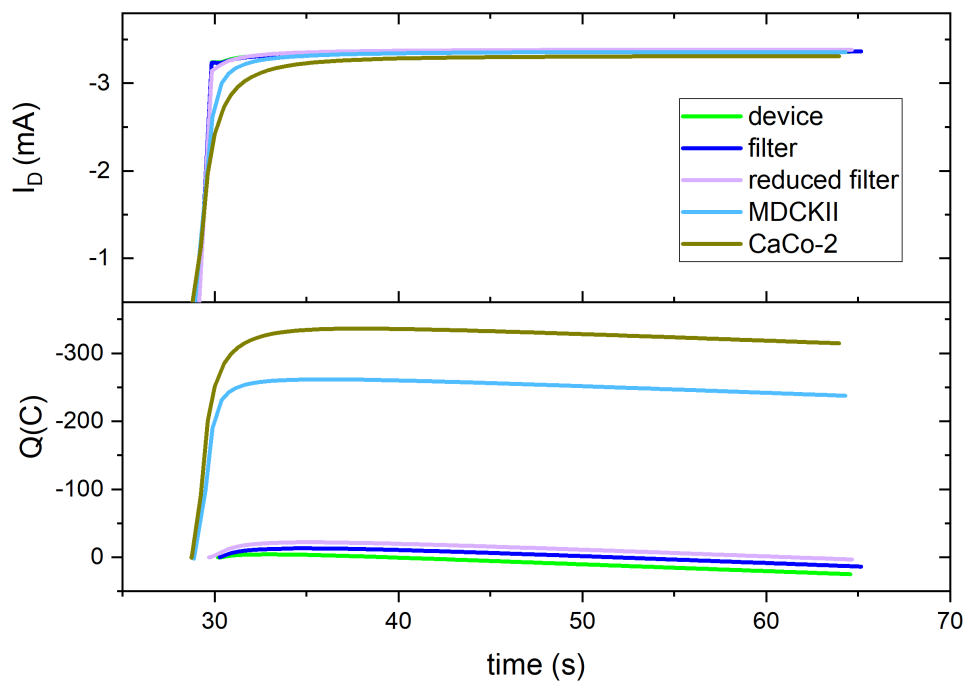


**Figure 14: Comparison of transient electronic current  $I_D$  and ionic charge density  $Q$  over time.**

The OECTs electronic current  $I_D$  and anionic charge density  $Q$  response to the removal of a 0.5 V  $V_G$  pulse are shown, particularly, the figure displays the recovery to steady-state.  $I_D$  and  $Q$  are monitored over time for barriers of varying impedance, including the device only, plane filter, reduced filter, MDCKII-, and CaCo-2 barrier tissue.

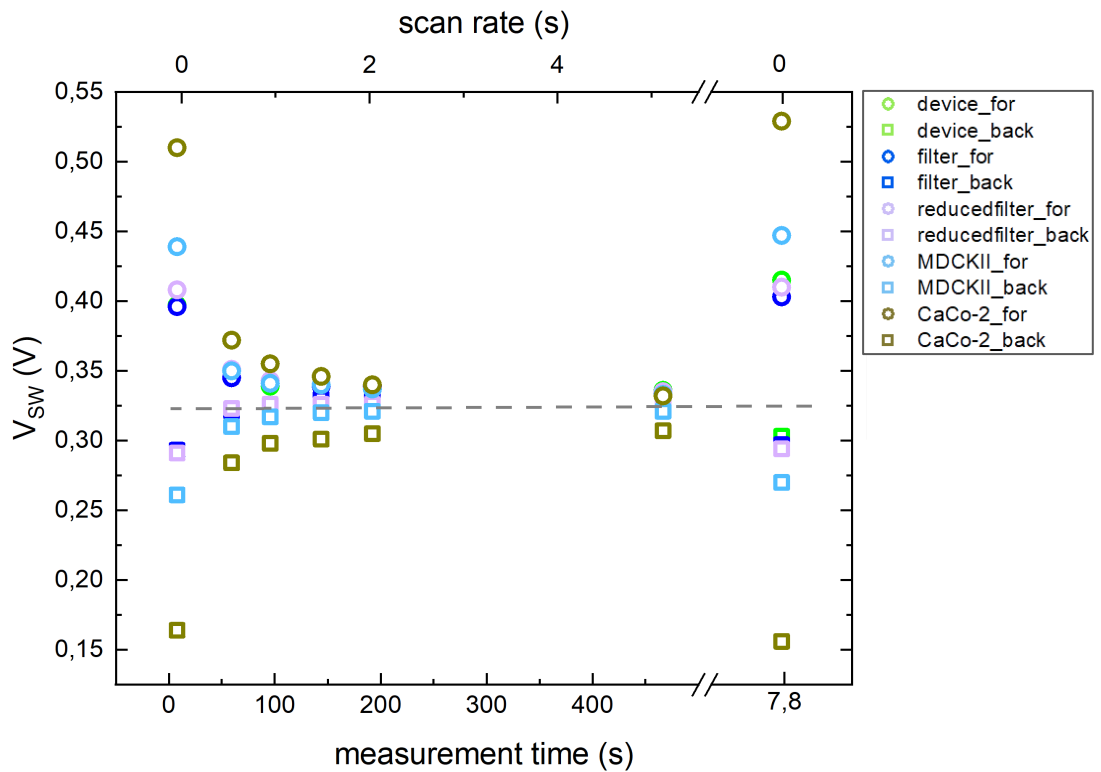


Figure 14 underlines the previous made conclusion that  $I_D$  reaches ON-state earliest for the device only and integrated plain filter. When a filter of reduced area is included, the ON-state is reached later, followed by the integrated MDCKII barrier tissue. Compared to all measurements, CaCo-2 barrier tissue reaches ON-state the latest. Additionally, it can be observed that the exponential incline for the curves of lower resistance is greater and has a steeper slope. Comparing the curves to anionic charge density, a similar exponential incline can be observed, whereby the incline is greater for barriers of higher resistance. It seems that steady-state condition for barriers of lower resistance is reached faster, corresponding to the observation for  $I_D$ . Both graphs start from saturation and respond to removal of  $V_G$  until ON-state of the transistor is reached and anions are in steady-state.

As a result it can be interpreted that once the  $V_G$  pulse is removed, anions release from accumulation at the gate and flow across the volume of electrolyte towards the channel. The anionic movement leads to an increase in negative  $Q$ . At the same time, cations are progressively extracted from the channel leading to an increase in  $I_D$ , until ON-state is reached. Whereas the response of  $I_D$  previously could be explained, the  $Q$  response is contrary to our expectations. It was expected that, once recovery from **Fig.13** is integrated,  $Q$  saturates at the same value for all systems with an increasing amplitude for barrier tissues of high resistance. However, further investigations must have to be carried out to identify the reason for this kind of anionic current. Yet, electronic and ionic current, particularly anion and cation motions, could be successfully monitored and we were able to conclude that transient response mostly depends on de-doping PEDOT:PSS.

### **4.2.2 Examine Transient Response Measurements in Current-Driven Organic Electrochemical Transistor Configuration with a changing scan rate**

To examine transient response of the OECT in the current-driven configuration,  $(V_{out}-V_{in})$ -transfer characteristics are performed with different integrated barriers (device only, plane filter, reduced filter, MDCKII- and CaCo-2 barrier tissue). Each of the measurements is performed for a varying scan rate [0; 0.5; 1; 1.5; 2; 5; 0] s. Besides the forward sweep, with  $V_{in}$  swept from negative to positive, a backward sweep is performed to extract all the cations from the channel. For analyzation,  $V_{SW}$  is plotted over total measurement time and scan rate in seconds. To assure device stability and validate the results, measurements are repeated for 0 s scan rate. For a stable measurement, it is expected that this value corresponds to the initial 0 s measurement.



**Figure 15: Transient Response of the OECT in the Current-Driven Configuration with different integrated barriers.**

The figure displays the  $(V_{out}-V_{in})$ -transfer characteristics of the OECT in the current-driven configuration. As figure-of-merit, the switching voltage  $V_{SW}$  is plotted over measurement time and corresponding scan rate. Measurement is performed for [0; 0.5; 1; 1.5; 2; 5; 0] s scan rate.

Clearly a distinction between the barriers can be made for a fast measurement with a sweep delay of 0 s. The  $V_{SW}$  is the highest for the CaCo-2 barrier tissue, which offers the highest impedance and vice versa. For the backward sweep,  $V_{SW}$  is lowest for the barrier with the highest impedance, indicating a high hysteresis for this specific system. The measurement points for the device only and plane filter are overlapping at some points, it can be said that these systems result in the lowest  $V_{SW}$  and show the smallest hysteresis. With increasing sweep delay,  $V_{SW}$  nears  $\sim 0.32$  V for each system, almost no distinction can be made between the different barriers. The 0 s reference measurement results are consistent with the initial values, the measurement can be considered as stable and correct.

Concluding from these results, the  $V_{SW}$  is transient and, therefore, the sensitivity of the OECT in the current-drive configuration is transient. Regarding the fast measurement, the device does not respond to dedoping as fast as to doping. Therefore, not all cations are extracted from the channel, leading to a high hysteresis. Saturation can't be reached and the OECT operates in linear regime. For slow measurements, the OECT operates in saturation regime. The ions have enough time to react to the gate pulse and factually migrate into the channel until saturation is reached, reflecting the actual response to  $V_G$ .

Regarding the OECT as an impedance sensor for barrier tissues, it can be concluded that it is essential to use a short scan rate. Especially when it comes to monitoring dynamic processes within barrier tissues, the short scan rate is important to detect these variations.

## 4.1 Biological Application of the OECT in the Current-Driven Configuration

Here, the OECT was investigated on dynamically sensing a reversible TJ opening due to exposure of EDTA in 1 mM and 10 mM concentrations.

To validate the expression of TJs in CaCo-2 and MDCKII barrier tissues, occludin and zonulin are representatively stained with a fluorochrome marked primary antibodies. The TJ modulation is performed after. Results are quantified by the figure-of merit  $V_{sw}$ , monitored over time.

### 4.1.1 Immunofluorescence Staining of Tight Junctional Proteins

Occludin and zonulin expression was observed by confocal laser scanning microscopy (cLSM) analysis, to representatively verify TJs in CaCo-2 and MDCKII barrier tissues. In order to visualise the morphology of the cell and demonstrate the location of TJs, the nucleus was also stained and merged with TJ-zoom images.

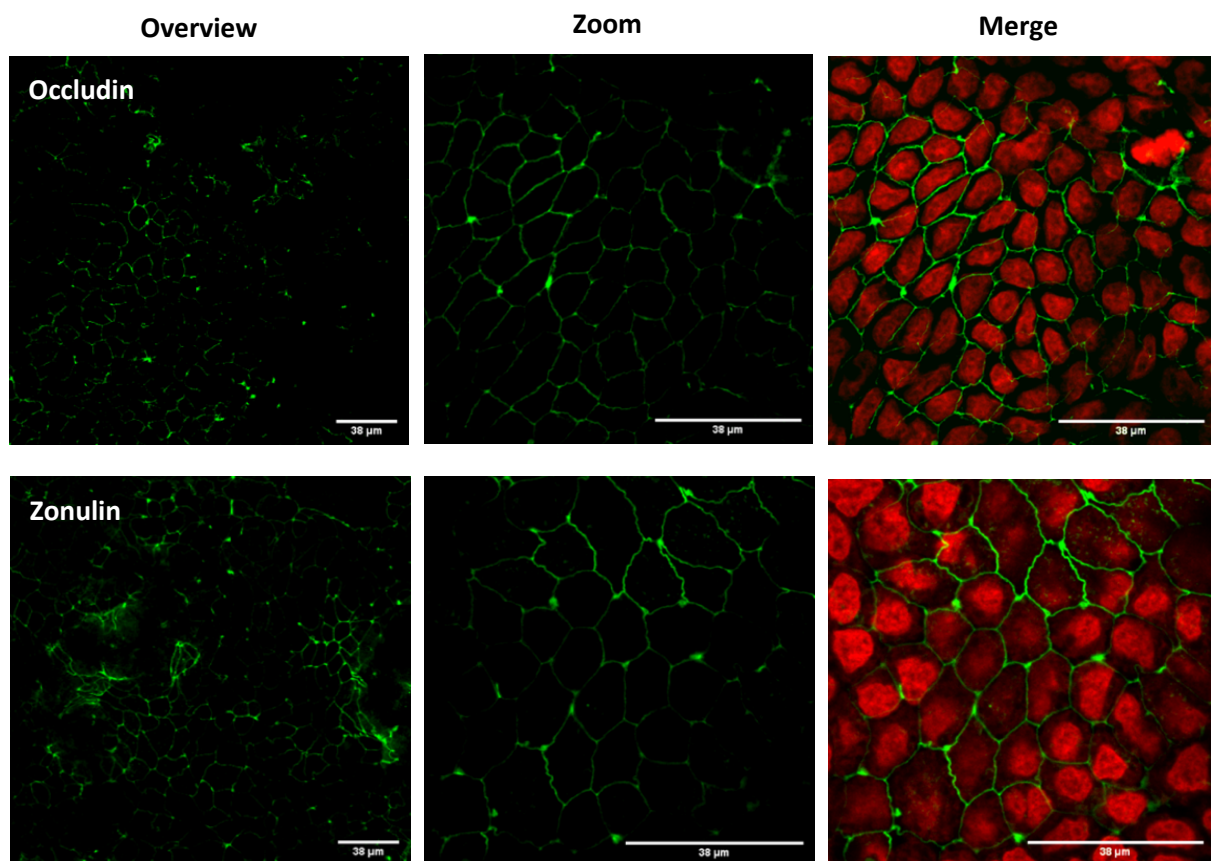


**Figure 16: CLSM images of CaCo-2 barrier tissue.**

CaCo-2 cells were cultivated and stained on ibidi coverslips. The cells were occludin and zonulin-stained. The nucleus was stained with DRAQ5 for determination of cell morphology. For each staining, an overview, a zoom, and a merge of TJ and nucleus staining is shown

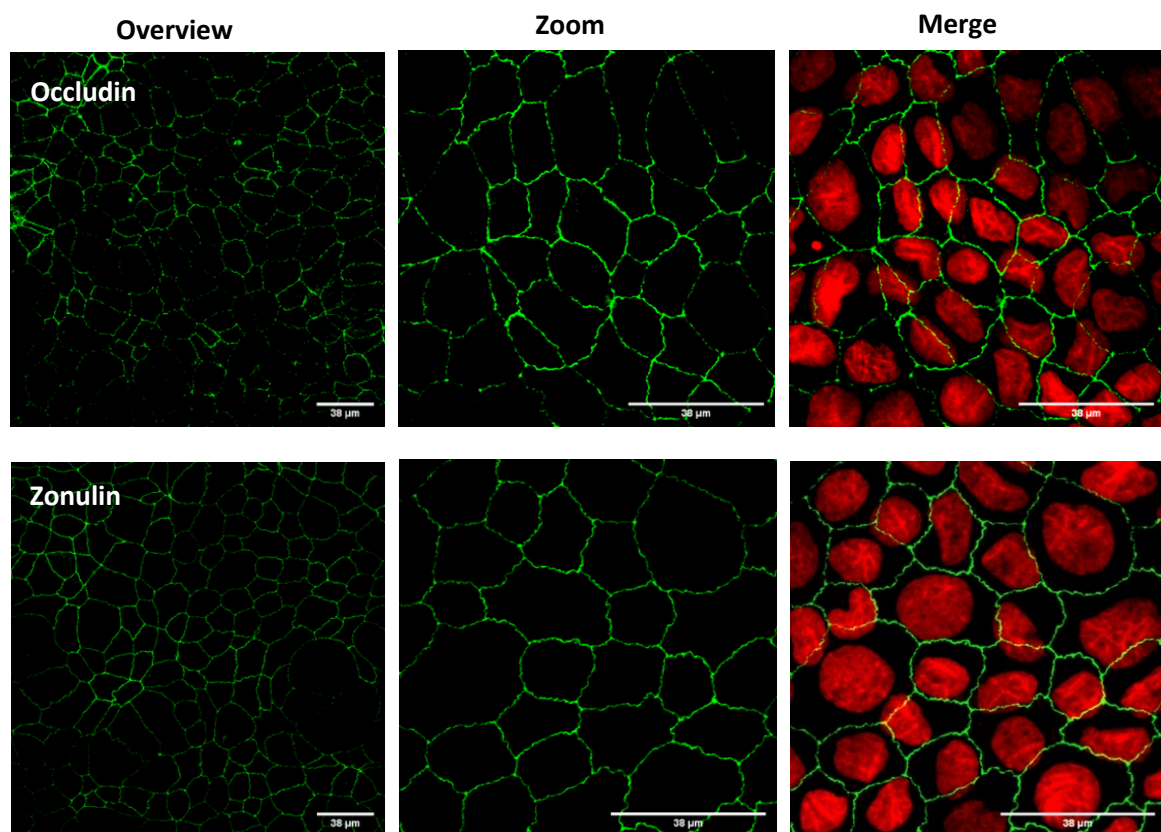


**Figure 17: CLSM Images of MDCKII barrier tissue**

MDCKII cells were cultivated and stained on ibidi coverslips. The cells were occludin and zonulin-stained. The nucleus was stained with DRAQ5 for determination of cell morphology. For each staining, an overview, a zoom, and a composition of TJ and nucleus staining is shown.

Occludin and zonulin appear as continuous network for MDCKII barrier tissues, located at cell-cell boundaries. In CaCo-2 barrier tissues, TJs appear rather inhomogeneous and especially zonulin seems diffuse in some parts of the overview. Since occludin and zonulin staining has been successful in the past<sup>[35,66,67]</sup>, the demonstrated results lead to the assumption that either cells have been damaged during pipetting or the staining has not succeeded. The dark spots in the CaCo-2 staining could also be an indication of bleaching due to the high intensity of the stimulating laser, during zoom-image recording.

Interestingly, zonulin and occluding seem wavy in both barrier tissues, which might be an indication for dynamic processes in the system before fixation. In comparison, a less dynamic cell membrane appears sharp edged and stiff under the CLSM.<sup>[68]</sup> Further, the nuclei seem tightly packed for CaCo-2 cells, indicating a tight barrier tissue. Nuclei of MDCKII cells are distant from each other, indicating a more leaky barrier tissue. These results correlated with literature, where TEER is  $\sim 400 \Omega\text{cm}^2$  for CaCo-2 and  $\sim 100 \Omega\text{cm}^2$  for MDCKII barrier tissue.

In conclusion, the expression of TJs has been successfully demonstrated and the assumption of a tighter CaCo-2 barrier and a less tight MDCKII barrier has been confirmed.

#### 4.1.2 Detecting Tight Junction Modulation of CaCo2 and MDCK II with the OECT

Here, the epithelial barrier tissue integrity of MDCKII and CaCo-2 barrier tissues under influence of EDTA in a concentration of 10mM and 1mM is demonstrated. To analyze electrical response of the barrier tissues, the shifting of ( $V_{out} - V_{in}$ )-transfer characteristics were quantified by the switching voltage  $V_{SW}$ , which is monitored over time.

To assure device stability, ( $V_{out} - V_{in}$ )-transfer characteristics were measured 1,5 h with an integrated PDMS-coated filter prior to membrane stability. After membrane stability is guaranteed (grey area; **Fig.18,19**), cells are exposed to EDTA (green area; **Fig.18,19**). The electrolyte is exchanged basal and apical after EDTA exposure of approximately 30 min, whereby 0.5 mL EMEM is kept in the basal compartment for experiments with CaCo-2 cells. The TJ recovery is monitored overnight (blue area; **Fig.18,19**).

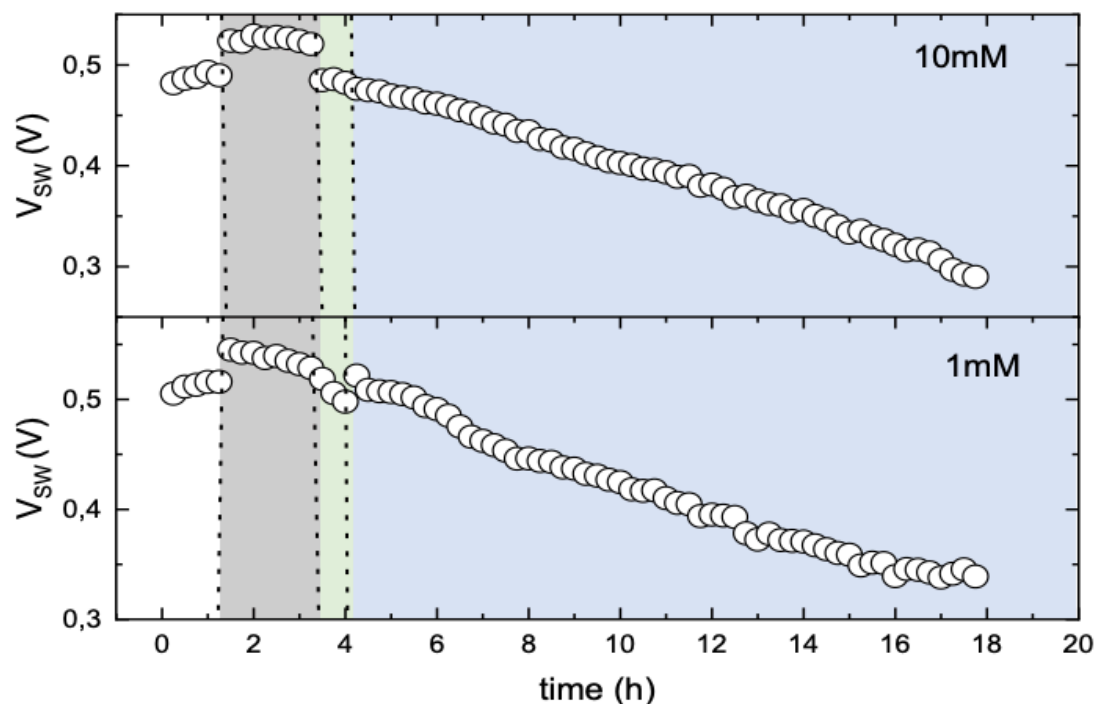


**Figure 18: Concentration effect of TJ modulator to MDCKII cells, measured with the current-driven OECT.**

Monitoring extracted  $V_{SW}$  of all ( $V_{out} - V_{in}$ )- transfer characteristics over time of the experiment for MDCKII barrier tissue, exposed to 1 mM and 10 mM EDTA. Dashed lines help to distinguish the experimental steps. White colored area shows  $V_{SW}$  in absence of barrier tissue and the grey area, in presence of a barrier tissue. Area with the green background displays  $V_{SW}$  during exposure to EDTA and area with the blue background shows the  $V_{SW}$  during recovery of the barrier tissue, after exchanging the EMEM, respectively.

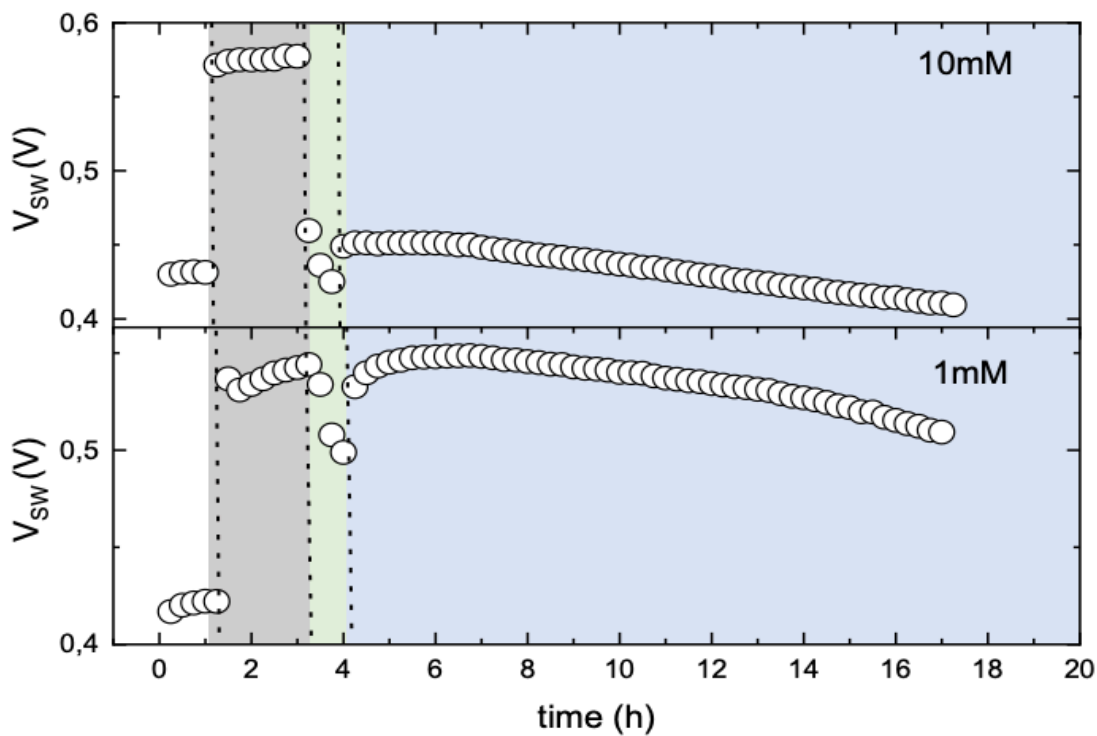


**Figure 19: Concentration effect of TJ modulator EDTA to CaCo-2 cells, measured with the current-driven OECT.**

Monitoring extracted  $V_{SW}$  of all ( $V_{out} - V_{in}$ )- transfer characteristics over time of the experiment for CaCo-2 barrier tissue, exposed to 1 mM and 10 mM EDTA. Dashed lines help to distinguish the experimental steps. White colored area shows  $V_{SW}$  in absence of barrier tissue and the grey area, in presence of a barrier tissue. Area with the green background displays  $V_{SW}$  during exposure to EDTA and area with the blue background shows the  $V_{SW}$  during recovery of the barrier tissue, after exchanging the EMEM, respectively.

Comparing the results, a significant difference between the integrated barriers as well as a concentration dependent response to EDTA exposure becomes clear.

Once an intact barrier tissue is introduced to the OECT, the  $V_{SW}$  instantly increases to a value of  $\sim 0.48 - 0.5$  V for MDCKII and  $\sim 0.55 - 0.58$  V for CaCo-2 barrier tissue, as the cell layers act as barrier for ions and a higher  $V_{in}$  is needed. The voltage increase for an integrated CaCo-2 layer is clearly greater than for MDCKII tissue, indicating that the CaCo-2 barrier tissue is tighter than MDCKII barrier tissue and, thus, ion flux is significantly more impaired. Membrane stability is assured for both types of tissues. In comparison, the  $V_{SW}$  value of the device with integrated plane filter (white area; **Fig.18,19**) is approximately  $\sim 0.5$  V for the experiments with MDCKII barrier tissue and  $\sim 0.43$  V for experiments with CaCo-2 as barrier tissue.

When exposing MDCKII barrier tissue to 10 mM EDTA, a sudden voltage drop to the value of the plane filter can be detected, which indicates a TJ opening and the loss of MDCKII's barrier functionality. For the whole time of EDTA exposure, this voltage value stays constant and also after exchanging the whole volume of EMEM apical and basal,  $V_{SW}$  doesn't significantly change. It is assumable that the

EDTA dose had a toxic effect on the barrier tissue, since an instant  $V_{SW}$  drop and no TJ recovery is detected.<sup>[27]</sup> The high EDTA concentration might have led to shrinking of the cells or cell detachment from the filter, since cell-matrix-junctions are also  $Ca^{2+}$  dependent.<sup>[15]</sup> The TEER value of the barrier tissue was  $1120 \Omega$  before and  $144 \Omega$  after the measurement, which underlines the assumption of irreversible loss of barrier functionality. From hour 6 onwards, a slight drop in  $V_{SW}$  can be observed that extends to the end of the experiment. Over a time frame of 12 h, from hour 6 of the experiment to hour 18, the  $V_{SW}$  value drops from  $\sim 0.46$  V to about  $\sim 0.28$  V. This shift seems to be unrelated to the barrier tissue, but to the device stability, as the value even decreases below the initially measured device stability value (white area; **Fig.19**).

Exposure to 1mM EDTA, causes a rather slow drop in  $V_{SW}$ . The first of three measurement points is near the value of the stable barrier, whereas the third measurement point nears the voltage value of the plane filter, demonstrating a time-dependent TJ opening. After exchanging EMEM apical and basal,  $V_{SW}$  increases almost to the value of the stable barrier tissue, but drops instantly after the first measuring point. At this value, the measurement initially remains stable until hour 6 and then starts decreasing to  $\sim 0.34$  V, indicating scarce device stability. Since the TEER value of this MDCKII barrier tissue was  $983 \Omega$  before the experiment and  $750 \Omega$  after, a reversible TJ opening can be assumed, even though it does not correspond exactly to the initial value.

On introducing 10 mM EDTA to the intact CaCo-2 barrier tissue, a gradual  $V_{SW}$  decrease, to the value of the plane filter can be observed. After exchanging EMEM, the  $V_{SW}$  value increases to  $\sim 0.45$  V and stays stable until hour 6. From this point onwards, a slight drift towards 0.4 V can be observed. However, the measurement seems to be much more stable throughout the 20 h, than the experiment with the MDCKII barrier tissue. The TEER value for the CaCo-2 barrier tissue was  $7500 \Omega$  before the experiment and  $78 \Omega$  after, indicating an irreversible TJ modulation.

Exposure of CaCo-2 barrier tissue to 1 mM EDTA, has a slightly different effect. The  $V_{SW}$  decreases gradually to  $\sim 0.49$  V, which is significantly higher than the value of the plane filter. This could represent either a partial opening of TJs or an inhomogeneous calcium chelation.<sup>[58]</sup> After exchanging EMEM,  $V_{SW}$  increases to the pristine value of the intact barrier tissue and stays stable until hour 8. From then on the value undergoes a slight downward shift to  $\sim 0.52$  V. Here, the initial TEER value amounts  $5620 \Omega$  and  $6320 \Omega$  after the measurement.

Concluding, it can be said that upon a decrease of extracellular  $Ca^{2+}$ , caused by the impact of EDTA, the OECT senses the breach in barrier tissue rapidly. On addition of 1mM and 10mM EDTA a concentration dependent reduction in  $V_{SW}$  can be observed, indicating a growing TJ disruption with higher concentration. The loss of barrier functionality further depends on the tightness of the respective cell barrier. While a high dose of EDTA has a toxic effect on MDCKII barrier tissue (TEER  $\sim 1000 \Omega$ ), leading to TJ disruption, the same concentration of EDTA leads to a reversible TJ opening on exposure to CaCo-



2 barrier tissue (TEER  $\sim$ 6000  $\Omega$ ). J.Ye et al already proposed in 2012 that high concentrations of EDTA have genotoxic effects on corneal epithelial cells, leading to apoptosis of the cells.<sup>[69]</sup> This proposal might be an explanation for irreversible loss of barrier functionality for both, MDCKII and CaCo-2 cells, after incubation with 10mM EDTA. It is conceivable that the effect of TJ disruption occurred rather slow for CaCo-2 barrier tissue, due to its greater intercellular sealing.

1mM EDTA exposure shows a reversible TJ opening, whereby results are different for both barrier tissues: while exposure to MDCKII barrier tissue leads to a complete loss of barrier functionality, the same concentration seems to not even open all TJs in CaCo-2 barrier tissue. Regarding the latter, the TEER value even increased, meaning that the cells metabolism wasn't harmed at all and the cell was able proliferate and form TJs as under optimal cell culture conditions.

Furthermore, the TJ opening seems to happen rather fast, in comparison to the recovery. This rapid decrease can be explained with the chelation of  $\text{Ca}^{2+}$  bound E-cadherin molecules in between adjacent cells, which is followed by endocytosis of these molecules, causing a displacement of proteins like occludin and zonulin. In order to recover TJs, new molecules must be transported to the cell membrane, which occurs on a longer timescale.<sup>[15]</sup>

The results give a little more insight into the function of TJ and their response to EDTA as a TJ modulator. Still, TJs are dynamic structures, regarding their morphology and physiological behavior, which is why detailed information is still deficient.<sup>[56]</sup>

Considering OECT operation, the results show that the utility of the OECT is a powerful method for studies on cell layer integrity and general toxicology of cells. The results correspond to the measured TEER values, which served as reference. Compared to research results on TJ modulation with other techniques, such as immunofluorescence staining<sup>[70]</sup> and TEER<sup>[70]</sup> measurements, the OECT provides high temporal resolution, dynamic monitoring of cell layer integrity and higher sensitivity. Contrary to the expectations, the device is not stable over the whole time of measurement, at least for experiments with MDCKII barrier tissues. Before and after the four experiments, transfer-characteristics were measured, showing a decrease in  $I_D$  after MDCKII measurements. At this point it is interesting to note that for measurements with MDCKII barrier tissue, a different device was used and the entire medium was replaced apical and basal, whereas for the measurements with CaCo-2 barrier tissue, 0.5 mL was left basal above the channel, i.e. only 1 mL EMEM was exchanged after EDTA exposure. However, transfer characteristics after CaCo-2 experiments show a stable  $I_D$  and experimental results (**Fig.14b**) a rather negligible downward shift. This leads to the assumption of either a manufacturing defect of the device used for MDCKII measurement. On the other hand it might be that the channel should have the same condition during the individual experimental steps in order to obtain a stable measurement. To find out more, further investigations need to be carried out.



## 5. Summary and Outlook

The strongly emerging field of bioelectronics has emerged the OECT as undefeated winner in terms of signal amplification, sensitivity, and biocompatibility at low cost fabrication. In this thesis the transient response of the OECT has been investigated with the aim of biosensing application, particularly improved assessment of tight junction modulation.

Transient response measurement with the OECT in the standard configuration successfully displayed cationic and anionic ion flux upon an applied gate voltage pulse. We were able to conclude that the transient current mainly relies on dedoping PEDOT:PSS, or rather hole extraction. The anionic movement in the system were contrary to our expectations and could not be clearly understood. In order to get more insight into the anionic behavior, further investigations have to be made.

By monitoring the ( $V_{out}-V_{in}$ )-transfer characteristics of the current-driven OECT for varying scan rates, it became evident that the  $V_{sw}$ , as figure-of-merit, is transient. Most importantly, we concluded that in order to carry out sensitive measurements with an integrated barrier tissue, it is essential to use a low scan rate.

The next chapter took up this issue by monitoring TJ modulation of MDCKII- and CaCo-2 barrier tissues with the OECT in the current-driven configuration successfully. Although measurements for MDCKII barrier tissue seem rather unstable, we were able to obtain interesting information from the measurements. The results show that EDTA has a rather toxic effect in a high dose of 10 mM, whilst exposure of 1 mM EDTA to the barrier tissues displayed a reversible TJ modulation. Further, the EDTA had a stronger effect on MDCKII- than on CaCo-2 barrier tissues, which can be explained with the lower TEER value.

Concluding, the results prove the suitability of the OECT as a dynamic biosensor to monitor reversible TJ modulation and opens up the window for time- and concentration-dependent investigations on TJ modulators. The current-driven OECT at low scan rates has an enhanced sensitivity for the integrity of a barrier tissue, which is applicable in electrophysiology, further it sensed the barrier disruption, which is particular necessary for toxicological studies. In addition, the current-driven OECT sensed the recovery of tight junctions and by that proves suitability for studying drug delivery systems.

Nevertheless, the technique is not yet fully developed, and not all internal mechanisms are understood. Considering device stability, further investigations have to be made to assure reproducibility and equally efficient performance for each device.

Moreover, it would be interesting to establish a mathematical model for the ion flux across an integrated barrier. In this way, it would be easy to make predictions about ion behavior and perhaps also to understand the transient anion flux. In this regard, Skinner et al published a paper in 1993, which is applicable to our approach.<sup>[71]</sup>

Considering practical application, the technique would be easier in handling, if the  $V_{sw}$  would be instantly converted to resistance, respective to the TEER of the barrier tissue. Since a correlation between  $V_{sw}$  and TEER could be observed from the results, this is in any case a further step into establishment of advantageous properties of the OECT.

However, the OECT in the current-driven configuration offers a broad range of advantages that make it applicable in pharmaceutical research and replace morally questionable animal studies for e.g. toxicological profiling.

## 6. Appendix

### Application of the Statistical Rate Approach for ion permeation; Skinner et.al 1993

1. Deriving (9)  $j = K_x \left( \frac{K_e [A][B]}{[C][D]} - \frac{[C][D]}{K_e [A][B]} \right)$ , with

$$(2) j = K_x (\delta - \delta^{-1})$$

$$(3) j = \exp\left(\frac{\mu_A + \mu_B - \mu_C - \mu_D}{RT}\right)$$

$$(7) \mu_\gamma = \mu_\gamma^0(T, P) + RT \ln(\alpha_\gamma)$$

$$(8) \alpha_\gamma = \alpha_\gamma[\gamma]$$

$$\Leftrightarrow j = K_x \left( \exp \frac{\mu_A^0 + \mu_B^0 - \mu_C^0 - \mu_D^0 + RT \ln[A] + RT \ln[B] - RT \ln[C] - RT \ln[D]}{RT} \right. \\ \left. - \frac{1}{\exp \frac{\mu_A^0 + \mu_B^0 - \mu_C^0 - \mu_D^0 + RT \ln[A] + RT \ln[B] - RT \ln[C] - RT \ln[D]}{RT}} \right)$$

$$\Leftrightarrow j = K_x \left( \exp \frac{\mu_A^0 + \mu_B^0 - \mu_C^0 - \mu_D^0 + RT (\ln[A] + \ln[B]) - RT (\ln[C] + \ln[D])}{RT} \right. \\ \left. - \frac{1}{\exp \frac{\mu_A^0 + \mu_B^0 - \mu_C^0 - \mu_D^0 + RT (\ln[A] + \ln[B]) - RT (\ln[C] + \ln[D])}{RT}} \right)$$

$$\Leftrightarrow j = K_x \left( \exp \frac{\mu_A^0 + \mu_B^0 - \mu_C^0 - \mu_D^0}{RT} + \frac{RT (\ln[A] + \ln[B])}{RT} - \frac{RT (\ln[C] + \ln[D])}{RT} \right. \\ \left. - \frac{1}{\exp \frac{\mu_A^0 + \mu_B^0 - \mu_C^0 - \mu_D^0}{RT} + \frac{RT (\ln[A] + \ln[B])}{RT} - \frac{RT (\ln[C] + \ln[D])}{RT}} \right)$$

$$\leftrightarrow j = K_x \left( \frac{\exp \frac{\mu_A^0 + \mu_B^0 - \mu_C^0 - \mu_D^0}{RT} * \frac{\exp \frac{RT(\ln[A] + \ln[B])}{RT}}{\exp \frac{RT(\ln[C] + \ln[D])}{RT}}}{\frac{1}{\exp \frac{\mu_A^0 + \mu_B^0 - \mu_C^0 - \mu_D^0}{RT} * \frac{\exp \frac{RT(\ln[A] + \ln[B])}{RT}}{\exp \frac{RT(\ln[C] + \ln[D])}{RT}}}} \right)$$

$$\leftrightarrow j = K_x \left( \exp \frac{\mu_A^0 + \mu_B^0 - \mu_C^0 - \mu_D^0}{RT} * \frac{[A] * [B]}{[C] * [D]} - \frac{1}{\exp \frac{\mu_A^0 + \mu_B^0 - \mu_C^0 - \mu_D^0}{RT} * \frac{[A] * [B]}{[C] * [D]}} \right)$$

With  $K_e = \exp \frac{\mu_A^0 + \mu_B^0 - \mu_C^0 - \mu_D^0}{RT}$

$$\leftrightarrow j = \frac{K_e * [A] * [B]}{[C] * [D]} - \frac{1}{\frac{K_e [A] * [B]}{[C] * [D]}}$$

$$\leftrightarrow j = \frac{K_e * [A] * [B]}{[C] * [D]} - \frac{[C] * [D]}{K_e * [A] * [B]}$$

2. Deriving (20)  $\frac{[C_x]_{i, \text{equil}} \exp(\theta_x \phi_{\text{equil}}^{Ci})}{[X]_{i, \text{equil}} \exp(\theta_x \phi_{\text{equil}}^i)} = \frac{\alpha_x^i}{\alpha_x} \exp\left(\frac{\mu_x^{0,i} - \mu_x^0}{RT}\right)$

$$(21) \frac{[C_x]_{e, \text{equil}} \exp(\theta_x \phi_{\text{equil}}^{Ce})}{[X]_{e, \text{equil}} \exp(\theta_x \phi_{\text{equil}}^e)} = \frac{\alpha_x^e}{\alpha_x} \exp\left(\frac{\mu_x^{0,e} - \mu_x^0}{RT}\right), \text{ with}$$

$$(14) \mu_x^{Ci} = \mu_x^0(T, P) + RT \ln(\alpha_x^{Ci}) + z_x F \phi^{Ci}$$

$$(15) \mu_x^{Ce} = \mu_x^0(T, P) + RT \ln(\alpha_x^{Ce}) + z_x F \phi^{Ce}$$

$$(16) \mu_x^i = \mu_x^{0,i}(T, P) + RT \ln(\alpha_x^i) + z_x F \phi^i$$

$$(17) \mu_x^e = \mu_x^{0,e}(T, P) + RT \ln(\alpha_x^e) + z_x F \phi^e$$

$$(18) \theta_x = \frac{z_x F}{RT}$$

$$(19) \mu_x^i = \mu_x^{Ci} = \mu_x^{Ce} = \mu_x^e, \text{ for thermodynamic equilibrium}$$

$$\mu_x^{Ci} = \mu_x^i$$

$$\mu_x^{0,i} + RT * \ln(\alpha_x^{Ci}) + z_x F \phi^{Ci} = \mu_x^0 + RT * \ln(\alpha_x^i) + z_x F \phi^i$$

$$\begin{aligned}
 & RT*\ln(\alpha_x^{Ci}) + z_x F\phi^{Ci} = \mu_x^0 - \mu_x^{0,i} + RT*\ln(\alpha_x^i) + z_x F\phi^i \\
 & RT*\ln(\alpha_x^{Ci}) + \ln[C_x]_{i, \text{equil}} + z_x F\phi^{Ci} - z_x F\phi^i = \mu_x^0 - \mu_x^{0,i} + RT*\ln(\alpha_x^i) + \ln[X]_{i, \text{equil}} \\
 & \frac{RT*\ln(\alpha_x^{Ci}) + \ln[C_x]_{i, \text{equil}} + z_x F\phi^{Ci} - z_x F\phi^i}{RT} = \frac{\mu_x^0 - \mu_x^{0,i} + RT*\ln(\alpha_x^i) + \ln[X]_{i, \text{equil}}}{RT} \\
 & \frac{RT*(\ln(\alpha_x^{Ci}) - \ln(\alpha_x^i) + \ln[C_x]_{i, \text{equil}} - \ln[X]_{i, \text{equil}}) + z_x F\phi^{Ci} - z_x F\phi^i}{RT} = \frac{\mu_x^0 - \mu_x^{0,i}}{RT} \\
 & \exp \frac{RT*(\ln(\alpha_x^{Ci}) - \ln(\alpha_x^i) + \ln[C_x]_{i, \text{equil}} - \ln[X]_{i, \text{equil}}) + z_x F\phi^{Ci} - z_x F\phi^i}{RT} = \exp \frac{\mu_x^0 - \mu_x^{0,i}}{RT} \\
 & \exp \frac{RT*\ln(\alpha_x^{Ci}) - \ln(\alpha_x^i)}{RT} * \exp \frac{RT*\ln[C_x]_{i, \text{equil}} * \ln[X]_{i, \text{equil}}}{RT} * \exp \frac{z_x F\phi^{Ci} - z_x F\phi^i}{RT} = \exp \frac{\mu_x^0 - \mu_x^{0,i}}{RT} \\
 & \frac{\alpha_x^{Ci}}{\alpha_x^i} * \frac{[C_x]_{i, \text{equil}}}{[X]_{i, \text{equil}}} * \exp \frac{z_x F\phi^{Ci} - z_x F\phi^i}{RT} = \exp \frac{\mu_x^0 - \mu_x^{0,i}}{RT} \\
 & \frac{\alpha_x^{Ci}}{\alpha_x^i} * \frac{[C_x]_{i, \text{equil}} * \exp(\theta\phi^{Ci})}{[X]_{i, \text{equil}} * \exp(\theta\phi^i)} = \exp \frac{\mu_x^0 - \mu_x^{0,i}}{RT} \\
 & \frac{[C_x]_{i, \text{equil}} * \exp(\theta\phi^{Ci})}{[X]_{i, \text{equil}} * \exp(\theta\phi^i)} = \frac{\alpha_x^i}{\alpha_x^{Ci}} * \exp \frac{\mu_x^0 - \mu_x^{0,i}}{RT} \\
 & \leftrightarrow \frac{[C_x]_{e, \text{equil}} * \exp(\theta\phi^{Ce})}{[X]_{e, \text{equil}} * \exp(\theta\phi^e)} = \frac{\alpha_x^e}{\alpha_x^{Ce}} * \exp \frac{\mu_x^0 - \mu_x^{0,e}}{RT}
 \end{aligned}$$

3. Deriving (28)  $j_{i,Ci} = K_{i,Ci} \left[ -\frac{u(Ci)}{u(i)\beta_x^i} + \frac{u(i)\beta_x^i}{u(Ci)} \right]$   
 (29)  $j_{Ci,Ce} = K_{Ci,Ce} \left[ \frac{u(Ci)}{u(Ce)} - \frac{u(Ce)}{u(Ci)} \right]$   
 (30)  $j_{e,Ce} = K_{e,Ce} \left[ -\frac{u(Ce)}{u(e)\beta_x^e} + \frac{u(e)\beta_x^e}{u(Ce)} \right]$

, where

- (31)  $u(Ci) = [C_x]_i \exp(\theta\phi^{Ci})$   
 (32)  $u(Ce) = [C_x]_e \exp(\theta\phi^{Ce})$   
 (33)  $u(i) = [X]_i \exp(\theta\phi^i)$   
 (34)  $u(e) = [X]_e \exp(\theta\phi^e)$

, with

- (24)  $\beta_x^i = \frac{\alpha_x^i}{\alpha_x} \exp\left(\frac{\mu_x^{0,i} - \mu_x^0}{RT}\right)$   
 (25)  $\beta_x^e = \frac{\alpha_x^e}{\alpha_x} \exp\left(\frac{\mu_x^{0,e} - \mu_x^0}{RT}\right)$   
 (26)  $j_{1,2} = K_{1,2} (\delta_{1,2} - \delta_{1,2}^{-1})$   
 (27)  $\delta_{1,2} = \exp\left(\frac{\mu_x^1 - \mu_x^2}{RT}\right)$

$$j_{i,Ci} = K_{i,Ci} \left( \exp\left(\frac{\mu_x^i - \mu_x^{Ci}}{RT}\right) - \frac{1}{\exp\left(\frac{\mu_x^i - \mu_x^{Ci}}{RT}\right)} \right)$$

$$\begin{aligned}
j_{i,Ci} &= K_{i,Ci} \left( \exp \left( \frac{\mu_x^{0,i} + RT * \ln(\alpha_x^i) + z_x F \phi^i - \mu_x^0 - RT * \ln(\alpha_x^{Ci}) - z_x F \phi^{Ci}}{RT} \right) \right. \\
&\quad \left. - \frac{1}{\exp \left( \frac{\mu_x^{0,i} + RT * \ln(\alpha_x^i) + z_x F \phi^i - \mu_x^0 - RT * \ln(\alpha_x^{Ci}) - z_x F \phi^{Ci}}{RT} \right)} \right) \\
j_{i,Ci} &= K_{i,Ci} \left( \exp \left( \frac{\mu_x^{0,i} - \mu_x^0 + RT * (\ln(\alpha_x^i) + \ln[X]_i - \ln(\alpha_x^{Ci}) + [C_x]_i) + z_x F \phi^i - z_x F \phi^{Ci}}{RT} \right) \right. \\
&\quad \left. - \frac{1}{\exp \left( \frac{\mu_x^{0,i} - \mu_x^0 + RT * (\ln(\alpha_x^i) + \ln[X]_i - \ln(\alpha_x^{Ci}) + \ln[C_x]_i) + z_x F \phi^i - z_x F \phi^{Ci}}{RT} \right)} \right) \\
j_{i,Ci} &= K_{i,Ci} \left( \exp \left( \frac{\mu_x^{0,i} - \mu_x^0}{RT} \right) * \exp(\ln(\alpha_x^i) + \ln[X]_i - \ln(\alpha_x^{Ci}) + \ln[C_x]_i) * \exp \left( \frac{z_x F \phi^i - z_x F \phi^{Ci}}{RT} \right) \right. \\
&\quad \left. - \frac{1}{\exp \left( \frac{\mu_x^{0,i} - \mu_x^0}{RT} \right) * \exp \left( \frac{RT * (\ln(\alpha_x^i) + \ln[X]_i - \ln(\alpha_x^{Ci}) + \ln[C_x]_i)}{RT} \right) * \exp \left( \frac{z_x F \phi^i - z_x F \phi^{Ci}}{RT} \right)} \right) \\
j_{i,Ci} &= K_{i,Ci} \left( \exp \left( \frac{\mu_x^{0,i} - \mu_x^0}{RT} \right) * \frac{\alpha_x^i [X]_i}{\alpha_x^{Ci} [C_x]_i} * \exp \left( \frac{z_x F \phi^i - z_x F \phi^{Ci}}{RT} \right) \right. \\
&\quad \left. - \frac{1}{\exp \left( \frac{\mu_x^{0,i} - \mu_x^0}{RT} \right) * \frac{\alpha_x^i [X]_i}{\alpha_x^{Ci} [C_x]_i} * \exp \left( \frac{z_x F \phi^i - z_x F \phi^{Ci}}{RT} \right)} \right) \\
j_{i,Ci} &= K_{i,Ci} \left( \frac{\alpha_x^i}{\alpha_x^{Ci}} * \exp \left( \frac{\mu_x^{0,i} - \mu_x^0}{RT} \right) * \frac{[X]_i}{[C_x]_i} * \frac{\exp \left( \theta \frac{\phi^i}{RT} \right)}{\exp \left( \theta \frac{\phi^{Ci}}{RT} \right)} - \frac{1}{\frac{\alpha_x^i}{\alpha_x^{Ci}} * \exp \left( \frac{\mu_x^{0,i} - \mu_x^0}{RT} \right) * \frac{[X]_i}{[C_x]_i} * \frac{\exp \left( \theta \frac{\phi^i}{RT} \right)}{\exp \left( \theta \frac{\phi^{Ci}}{RT} \right)}} \right) \\
j_{i,Ci} &= K_{i,Ci} \left( \frac{[X]_i \exp(\theta \phi^i)}{[C_x]_i \exp(\theta \phi^i)} * \frac{\alpha_x^i}{\alpha_x^{Ci}} * \exp \left( \frac{\mu_x^{0,i} - \mu_x^0}{RT} \right) - \frac{1}{\frac{[X]_i \exp(\theta \phi^i)}{[C_x]_i \exp(\theta \phi^i)} * \frac{\alpha_x^i}{\alpha_x^{Ci}} * \exp \left( \frac{\mu_x^{0,i} - \mu_x^0}{RT} \right)} \right)
\end{aligned}$$



$$j_{i,ci} = K_{i,ci} \left( \frac{[X]_i \exp(\theta\phi^i)}{[C_x]_i \exp(\theta\phi^i)} * \beta_x^i - \frac{1}{\frac{[X]_i \exp(\theta\phi^i)}{[C_x]_i \exp(\theta\phi^i)} * \beta_x^i} \right)$$

$$(28) j_{i,ci} = K_{i,ci} \left( -\frac{u(ci)}{u(i)\beta_x^i} + \frac{u(i)\beta_x^i}{u(ci)} \right)$$

$$(30) \leftrightarrow j_{e,ce} = K_{e,ce} \left( -\frac{u(ce)}{u(e)\beta_x^e} + \frac{u(e)\beta_x^e}{u(ce)} \right)$$

$$j_{ci,ce} = K_{ci,ce} \left( \exp\left(\frac{\mu_x^{ci} - \mu_x^{ce}}{RT}\right) - \frac{1}{\exp\left(\frac{\mu_x^{ci} - \mu_x^{ce}}{RT}\right)} \right)$$

$$j_{ci,ce} = K_{ci,ce} \left( \exp\left(\frac{\mu_x^0 + RT * \ln(\alpha_x^{ci}) + z_x F \phi^{ci} - \mu_x^0 - RT \ln(\alpha_x^{ce}) - z_x F \phi^{ce}}{RT}\right) \right.$$

$$\left. - \frac{1}{\exp\left(\frac{\mu_x^0 + RT * \ln(\alpha_x^{ci}) + z_x F \phi^{ci} - \mu_x^0 - RT * \ln(\alpha_x^{ce}) - z_x F \phi^{ce}}{RT}\right)} \right)$$

$$j_{ci,ce} = K_{ci,ce} \left( \exp\left(\frac{RT * (\ln(\alpha_x^{ci}) - \ln(\alpha_x^{ce})) + z_x F \phi^{ci} - z_x F \phi^{ce}}{RT}\right) \right.$$

$$\left. - \frac{1}{\exp\left(\frac{RT * (\ln(\alpha_x^{ci}) - \ln(\alpha_x^{ce})) + z_x F \phi^{ci} - z_x F \phi^{ce}}{RT}\right)} \right)$$

$$j_{ci,ce} = K_{ci,ce} \left( \exp\left(\frac{RT * (\ln(\alpha_x^{ci}) + \ln[C_x]_i - \ln(\alpha_x^{ce}) + \ln[C_x]_e) + z_x F \phi^{ci} - z_x F \phi^{ce}}{RT}\right) \right.$$

$$\left. - \frac{1}{\exp\left(\frac{RT * (\ln(\alpha_x^{ci}) + \ln[C_x]_i - \ln(\alpha_x^{ce}) + \ln[C_x]_e) + z_x F \phi^{ci} - z_x F \phi^{ce}}{RT}\right)} \right)$$

$$j_{ci,ce} = K_{ci,ce} \left( \frac{\exp(\ln(\alpha_x^{ci}) + \ln[C_x]_i - \ln(\alpha_x^{ce}) + \ln[C_x]_e) * \exp\left(\frac{z_x F \phi^{ci} - z_x F \phi^{ce}}{RT}\right)}{\exp(\ln(\alpha_x^{ci}) + \ln[C_x]_i - \ln(\alpha_x^{ce}) + \ln[C_x]_e) * \exp\left(\frac{z_x F \phi^{ci} - z_x F \phi^{ce}}{RT}\right)} - \frac{1}{\frac{\alpha_x^{ci} * [C_x]_i * \exp\left(\theta \frac{\phi^i}{RT}\right)}{\alpha_x^{ce} * [C_x]_e * \exp\left(\theta \frac{\phi^{ci}}{RT}\right)} - \frac{1}{\frac{\alpha_x^{ci} * [C_x]_i * \exp\left(\theta \frac{\phi^i}{RT}\right)}{\alpha_x^{ce} * [C_x]_e * \exp\left(\theta \frac{\phi^{ci}}{RT}\right)}}} \right)$$

→ assuming a single phase in the channel, with  $\alpha_x^{ci} = \alpha_x^{ce}$

$$j_{ci,ce} = K_{ci,ce} \left( \frac{\alpha_x^{ci} * [C_x]_i * \exp(\theta \phi^i)}{\alpha_x^{ce} * [C_x]_e * \exp(\theta \phi^{ci})} - \frac{\alpha_x^{ce} * [C_x]_e * \exp(\theta \phi^{ci})}{\alpha_x^{ci} * [C_x]_i * \exp(\theta \phi^i)} \right)$$

$$(29) \quad j_{ci,ce} = K_{ci,ce} \left( \frac{u(Ci)}{u(Ce)} - \frac{u(Ci)}{u(Ce)} \right)$$

## 7. References

1. Berggren, M. & Richter-Dahlfors, A. Organic bioelectronics. *Adv. Mater.* **19**, 3201–3213 (2007).
2. Rivnay, J., Owens, R. M. & Malliaras, G. G. The rise of organic bioelectronics. *Chem. Mater.* **26**, 679–685 (2014).
3. Yuk, H., Lu, B. & Zhao, X. Hydrogel bioelectronics. *Chem. Soc. Rev.* **48**, 1642–1667 (2019).
4. Simon, D. T., Gabrielsson, E. O., Tybrandt, K. & Berggren, M. Organic Bioelectronics: Bridging the Signaling Gap between Biology and Technology. *Chemical Reviews* vol. 116 13009–13041 (2016).
5. <https://www.humanbrainproject.eu/en/>. No Title.
6. I. Willner, E. K. *Bioelectronics: From theory to applications*. (2005).
7. Perlmutter, J. S. & Mink, J. W. Deep brain stimulation. *Annu. Rev. Neurosci.* **29**, 229–257 (2006).
8. Kim, S. H. *et al.* Precisely printable and biocompatible silk fibroin bioink for digital light processing 3D printing. *Nat. Commun.* **9**, 1–14 (2018).
9. Lu, B. *et al.* Pure PEDOT:PSS hydrogels. *Nat. Commun.* **10**, (2019).
10. Nikolou, M. & Malliaras, G. G. Applications of poly (3,4-ethylenedioxythiophene) doped with poly(styrene sulfonic acid) transistors in chemical and biological sensors. *Chem. Rec.* **8**, 13–22 (2008).
11. Proctor, C. M., Rivnay, J. & Malliaras, G. G. Understanding volumetric capacitance in conducting polymers. *J. Polym. Sci. Part B Polym. Phys.* **54**, 1433–1436 (2016).
12. Picca, R. A. *et al.* Ultimately Sensitive Organic Bioelectronic Transistor Sensors by Materials and Device Structure Design. *Adv. Funct. Mater.* **30**, 1–23 (2020).
13. Groenendaal, L., Jonas, F., Freitag, D., Pielartzik, H. & Reynolds, J. R. Poly(3,4-ethylenedioxythiophene) and its derivatives: past, present, and future. *Adv. Mater.* **12**, 481–494 (2000).
14. Fromherz, P. Semiconductor chips with ion, nerve cells and brain. *elsevier* **16**, 24–34 (2003).
15. Ramuz, M., Hama, A., Rivnay, J., Leleux, P. & Owens, R. M. Monitoring of cell layer coverage and differentiation with the organic electrochemical transistor. *J. Mater. Chem. B* **3**, 5971–5977 (2015).
16. Håkansson, A. *et al.* Effect of (3-glycidyloxypropyl)trimethoxysilane (GOPS) on the electrical properties of PEDOT:PSS films. *J. Polym. Sci. Part B Polym. Phys.* **55**, 814–820 (2017).
17. Lingstedt, L. V. *et al.* Effect of DMSO Solvent Treatments on the Performance of

- PEDOT:PSS Based Organic Electrochemical Transistors. *Adv. Electron. Mater.* **5**, 1–8 (2019).
18. Vosgueritchian, M., Lipomi, D. J. & Bao, Z. Highly conductive and transparent PEDOT:PSS films with a fluorosurfactant for stretchable and flexible transparent electrodes. *Adv. Funct. Mater.* **22**, 421–428 (2012).
  19. Shi, H., Liu, C., Jiang, Q. & Xu, J. Effective Approaches to Improve the Electrical Conductivity of PEDOT:PSS: A Review. *Adv. Electron. Mater.* **1**, (2015).
  20. Modarresi, M., Mehandzhiyski, A., Fahlman, M., Tybrandt, K. & Zozoulenko, I. Microscopic Understanding of the Granular Structure and the Swelling of PEDOT:PSS. *Macromolecules* **53**, 6267–6278 (2020).
  21. Kovalchuk, N. M., Trybala, A., Starov, V., Matar, O. & Ivanova, N. Fluoro- Vs hydrocarbon surfactants: Why do they differ in wetting performance? *Adv. Colloid Interface Sci.* **210**, 65–71 (2014).
  22. Palumbiny, C. M., Schlipf, J., Hexemer, A., Wang, C. & Müller-Buschbaum, P. The Morphological Power of Soap: How Surfactants Lower the Sheet Resistance of PEDOT:PSS by Strong Impact on Inner Film Structure and Molecular Interface Orientation. *Adv. Electron. Mater.* **2**, 1–9 (2016).
  23. Rivnay, J. *et al.* Organic electrochemical transistors. *Nature Reviews Materials* vol. 3 (2018).
  24. Ohayon, D. & Inal, S. Organic Bioelectronics: From Functional Materials to Next-Generation Devices and Power Sources. *Adv. Mater.* **32**, (2020).
  25. Lin, P., Yan, F., Yu, J., Chan, H. L. W. & Yang, M. The application of organic electrochemical transistors in cell-based biosensors. *Adv. Mater.* **22**, 3655–3660 (2010).
  26. Strakosas, X., Bongo, M. & Owens, R. M. The organic electrochemical transistor for biological applications. *J. Appl. Polym. Sci.* **132**, 1–14 (2015).
  27. Lingstedt, L. V. *et al.* Monitoring of Cell Layer Integrity with a Current-Driven Organic Electrochemical Transistor. *Adv. Healthc. Mater.* **8**, 1–7 (2019).
  28. White, H. S., Kittlesen, G. P. & Wrighton, M. S. Chemical Derivatization of an Array of Three Gold Microelectrodes with Polypyrrole: Fabrication of a Molecule-Based Transistor. *J. Am. Chem. Soc.* **106**, 5375–5377 (1984).
  29. Fraunhofer IPMS. No Title. <https://www.ipms.fraunhofer.de/de/research-development/end-of-line-test-substrates/ofet.html>.
  30. Owens, R. M. & Malliaras, G. G. Organic electronics at the interface with biology. *MRS Bull.* **35**, 449–456 (2010).
  31. Rivnay, J. *et al.* Organic electrochemical transistors. *Nat. Rev. Mater.* **3**, (2018).
  32. Jimison, L. H. *et al.* Measurement of barrier tissue integrity with an organic electrochemical transistor. *Adv. Mater.* **24**, 5919–5923 (2012).

33. Ghittorelli, M. *et al.* High-sensitivity ion detection at low voltages with current-driven organic electrochemical transistors. *Nat. Commun.* **9**, 1–10 (2018).
34. Axel M. Gressner, T. A. *Lexikon der Medizinischen Laboratoriumsdiagnostik.* (Springer, Berlin, Heidelberg, 2019). doi:<https://doi.org/10.1007/978-3-662-48986-4>.
35. Katharina Lieberth a, Maximilian Brückner a, b, Fabrizio Torricelli c, Volker Mailänder a, b, P. G. a and P. W. M. B. a\*. Monitoring Reversible Tight Junction Modulation with a Current-Driven Organic Electrochemical Transistor. (2020).
36. Karp, G. *Cell and Molecular Biology: Concepts and Experiments.* (Wiley-VCH Verlag).
37. <https://www.lecturio.de/magazin/histologie-zelle/>.
38. B.Alberts. *Molecular biology of the cell.* (Garland Science).
39. No Title. <https://www.yourgenome.org/facts/what-is-a-cell>.
40. No Title. <http://www.biologie-schule.de/eukaryoten.php>.
41. No Title. <https://www.kenhub.com/de/library/anatomie/einfuehrung-in-die-gewebelehre>.
42. No Title. <https://www.kenhub.com/de/library/anatomie/epithelgewebe>.
43. Francisco, S. Complexes in Various Epithelia. *J. Cell Biol.* 375–412.
44. Barrier, D. O. N. W. Function of Epithelia. *Society* 275–288 (1981).
45. González-Mariscal, L., Nava, P. & Hernández, S. Critical role of tight junctions in drug delivery across epithelial and endothelial cell layers. *Journal of Membrane Biology* vol. 207 55–68 (2005).
46. Suzuki, T. Regulation of intestinal epithelial permeability by tight junctions. *Cell. Mol. Life Sci.* **70**, 631–659 (2013).
47. Gonzalez-Mariscal, L. *Tight junctions.* (Landes Bioscience/Eurekah.com, 2006).
48. Deli, M. A. Potential use of tight junction modulators to reversibly open membranous barriers and improve drug delivery. *Biochim. Biophys. Acta - Biomembr.* **1788**, 892–910 (2009).
49. Fasano, A. Zonulin and its regulation of intestinal barrier function: The biological door to inflammation, autoimmunity, and cancer. *Physiol. Rev.* **91**, 151–175 (2011).
50. *EndOhm Tissue resistance measurement chambers for tissue culture cups World Precision Instruments INSTRUCTION MANUAL.* [www.wpiinc.com](http://www.wpiinc.com) (2013).
51. Manual v3.04 - cZs+.
52. Rivnay, J. *et al.* Organic electrochemical transistors for cell-based impedance sensing. *Appl. Phys. Lett.* **106**, (2015).
53. Howarth, A. G., Hughes, M. R. & Stevenson, B. R. Detection of the tight junction-

- associated protein ZO-1 in astrocytes and other nonepithelial cell types. *Am. J. Physiol. - Cell Physiol.* **262**, 461–469 (1992).
54. Greene, C. & Campbell, M. Tight junction modulation of the blood brain barrier: CNS delivery of small molecules. *Tissue Barriers* **4**, (2016).
  55. <https://www.webmd.com/vitamins/ai/ingredientmono-1032/edta>.
  56. Rothen-Rutishauser, B., Riesen, F. K., Braun, A., Günthert, M. & Wunderli-Allenspach, H. Dynamics of tight and adherens junctions under EGTA treatment. *J. Membr. Biol.* **188**, 151–162 (2002).
  57. Stuart, R. O. *et al.* Critical role for intracellular calcium in tight junction biogenesis. *J. Cell. Physiol.* **159**, 423–433 (1994).
  58. Tria, S., Jimison, L. H., Hama, A., Bongo, M. & Owens, R. M. Sensing of EGTA mediated barrier tissue disruption with an organic transistor. *Biosensors* **3**, 44–57 (2013).
  59. Cho, M. J., Thompson, D. P., Cramer, C. T., Vidmar, T. J. & Scieszka, J. F. The Madin Darby Canine Kidney (MDCK) Epithelial Cell Monolayer as a Model Cellular Transport Barrier. *Pharmaceutical Research: An Official Journal of the American Association of Pharmaceutical Scientists* vol. 6 71–77 (1989).
  60. Shuler, L. & Hickman, J. J. *TEER measurements in cells. Journal of Laboratory Automation* vol. 20 (2016).
  61. Chang, B. Y. & Park, S. M. Electrochemical impedance spectroscopy. *Annu. Rev. Anal. Chem.* **3**, 207–229 (2010).
  62. Hickman, J. Transepithelial/endothelial Electrical Resistance (TEER) theory and applications for microfluidic body-on-a-chip devices. *J. Rare Dis. Res. Treat.* **1**, 46–52 (2016).
  63. Faria, G. C., Duong, D. T. & Salleo, A. On the transient response of organic electrochemical transistors. *Org. Electron.* **45**, 215–221 (2017).
  64. Benson, K., Cramer, S. & Galla, H.-J. *Impedance-based cell monitoring: barrier properties and beyond*. <http://www.fluidsbarrierscns.com/content/10/1/5> (2013).
  65. Bernardis, D. A. & Malliaras, G. G. Steady-state and transient behavior of organic electrochemical transistors. *Adv. Funct. Mater.* **17**, 3538–3544 (2007).
  66. Ramadan, Q. & Jing, L. Characterization of tight junction disruption and immune response modulation in a miniaturized Caco-2/U937 coculture-based in vitro model of the human intestinal barrier. *Biomed. Microdevices* **18**, 1–9 (2016).
  67. Ling, X., Linglong, P., Weixia, D. & Hong, W. Protective effects of bifidobacterium on intestinal barrier function in LPS-induced enterocyte barrier injury of Caco-2 monolayers and in a rat NEC model. *PLoS One* **11**, 1–17 (2016).
  68. <https://www.micron.ox.ac.uk/people/Lothar>.
  69. Ye, J. *et al.* High molecular weight hyaluronan decreases oxidative DNA damage

- induced by EDTA in human corneal epithelial cells. *Eye* **26**, 1012–1020 (2012).
70. Tria, S., Jimison, L. H., Hama, A., Bongo, M. & Owens, R. M. Sensing of EGTA mediated barrier tissue disruption with an organic transistor. *Biosensors* **3**, 44–57 (2013).
71. Skinner, F. K., Ward, C. A. & Bardakjian, B. L. Permeation in ionic channels: a statistical rate theory approach. *Biophys. J.* **65**, 618–629 (1993).